IDEA League

Master of Science in Applied Geophysics

Research Thesis

Towards understanding the 3D infrasonic wavefield

Thaïsa van der Woude

August 24, 2016

TU Delft

Delft University of Technology

Royal Netherlands Meteorological Institute

Ministry of Infrastructure and the Environment

Towards understanding the 3D infrasonic wavefield

Master of Science Thesis

for the degree of Master of Science in Applied Geophysics at
Delft University of Technology
ETH Zürich
RWTH Aachen University
by

Thaïsa van der Woude

August 24, 2016

Department of Geoscience & Engineering · Delft University of Technology
Department of Earth Sciences · ETH Zürich
Faculty of Georesources and Material Engineering · RWTH Aachen University

Delft University of Technology

Printed in The Netherland

IDEA LEAGUE
JOINT MASTER'S IN APPLIED GEOPHYSICS

Delft University of Technology, The Netherlands
ETH Zürich, Switzerland
RWTH Aachen, Germany

Dated: *August 24, 2016*

Supervisor(s):

Prof. Dr. L.G. Evers

Ir. P.S.M. Smets

Committee Members:

Prof. Dr. L.G. Evers

Ir. P.S.M. Smets

Prof. C. Clauser

Abstract

In the evening of 2014, June 03, two explosions occurred at the MSPO-2 plant of Shell Moerdijk. The Cabauw infrasound array detected the infrasound generated by the blasts as two distinct signals. The distance between Shell Moerdijk and the Cabauw infrasound array is 40.5 km. This array is unique as it measures infrasound in 3D. The Fisher analysis is used to process the infrasound signals. The horizontal 2D Fisher analysis verifies the infrasound source to be Shell Moerdijk, and it shows an azimuthal deviation of 2.1° caused by the influence of tropospheric crosswinds. The Shell Moerdijk explosions are used as a case study to investigate the measurement of infrasound in 3D. The frequency of the signals detected at the tower has been observed to be lower than the frequency of the signals detected at the surface. A possible reason is that the infrasound signals propagate through small pipes before reaching the tower sensors. Consequently, a reduced coherency between the tower and ground signals exists. Due to this lack of coherency, the 3D Fisher analysis was not able to perform correctly. The signature of the infrasound waveform with altitude is examined in detail, obtained by the vertical measurement of infrasound. It is showing up- and down-going waves in both explosion signals which can only be seen in the 3D vertical measurements. Ray tracing confirms the existence of these different waves. In summary, this research shows the added value of measuring infrasound in 3D.

Acknowledgements

First of all, I would like to thank all the people who have participated in this project. Especially my supervisor at the KNMI, Prof. Dr. L.G. Evers, who helped me greatly during my thesis with his knowledge and expertise. Besides, Ir. P.S.M. Smets and Dr. J.D. Assink supported me with their knowledge of the theory and Matlab programming to complete my master thesis.

Delft University of Technology Thaïsa van der Woude

August 24, 2016

Contents

List of Figures

List of Tables

Acronyms

KNMI Koninklijk Nederlands Meteorologisch Instituut

2D two-dimensional

3D three-dimensional

CIA Cabauw Infrasound Array

CTBT Comprehensive Nuclear-Test-Ban Treaty

UTC Universal Time Coordinated

CEST Central European Summer Time

MSPO-2 plant the second Monomer-Styrene-and-Propylene-Oxide plant

RD Rijksdriehoeksmeting: X,Y in meters

GCS Geographic Coordinate System: in latitude and longitude

GT0 Ground Truth zero

IMS International Monitoring System

DPRK Democratic People's Republic of Korea

NE Nuclear Explosion

HE High (chemical) Explosion

ECMWF European Centre for Medium-Range Weather Forecasts

HARMONIE HIRLAM ALADIN Research on Mesoscale Operational NWP in Euromed

Cesar Cabauw experimental site for atmospheric research

FFT Fast Fourier Transform

Chapter 1

Introduction

1-1 General introduction to infrasound

Humans can hear sounds ranging from 20 - 20,000 Hz. It means that, for example, an explosion occurring at thousand miles away can not be heard by human ears. Sound waves are pressure waves that travel with the speed of sound, e.g., 343 m/s at 20° Celsius. Ultrasonic sound waves are waves at frequencies above 20,000 Hz and infrasonic sound waves at frequencies below 20 Hz ('ultra' and 'infra' are Latin words for respectively 'above' and 'below'). Both these sound waves are inaudible to humans, but many animals can hear them. Infrasonic waves have amplitudes of hundredths to tens of pascals (Evers, 2008). Another valuable property of infrasound is that is can travel over great distances due to the low-frequency content. Infrasound can be divided in near-infrasound, which is frequencies just below 20 Hz, and far-infrasound, which is frequencies below 1 Hz. Near-infrasound can be felt such as, e.g., the bass of audio systems (Bedard & Georges, 2000).

Infrasound is acoustic from 0.02-20 Hz. If the wavelength of the infrasound becomes too long, gravity affects the mass displacement in the atmosphere. Consequently, in the frequency range from 0.002-0.02 Hz, infrasound consists of acoustic-gravity waves, and gravity becomes the restoring force instead of pressure. When the frequency is decreasing, the propagation of these 'acoustic-gravity' waves is getting more dispersive and anisotropic. At a frequency of 0.002 Hz, gravity waves have completely taken over the acoustic-gravity waves. The frequency range of the infrasonic wavefield is, therefore, from 0.002 - 20 Hz (Note that gravity waves are not the same as the recent discovered gravitational waves which are 'ripples' in the fabric of space-time).

Pressure fluctuations of infrasonic sound waves are small with respect to the ambient pressure. These small pressure variations are detected by a low-frequency pressure sensor, a microbarometer, described in detail in section 2-1-1. Measurements with microbarometers are affected by the local pressure fluctuation of the atmosphere caused mainly by the wind. A single sensor usually can not distinguish between the small pressure variations of infrasound and non-acoustic pressure changes. Therefore, it is useful to apply filters based on the

characteristics of infrasound to filter out noise. For example, sounds wave have a coherency in space and time, where noise possesses this property much less. This difference forms the basis for the array processing, see section 2-1-4.

The interest for infrasonic wavefield started after the second World War and had its peak during the Cold War. During this time, it became necessary to detect, locate and classify nuclear activities at great distances, and infrasound detection was the perfect tool for this application. Since the 1970's, more and more focus is on the atmospheric infrasound. Questions about the structure of the infrasonic wavefield, the infrasonic source and the influence of the atmosphere on infrasound rose, and more research were performed. The atmosphere consists of different layers where the temperature and the wind increases and decreases changing the direction of infrasound propagation, see section 2-2-1. The interpretation of infrasound waves from distances can be difficult due to seasonal and geographic variations in wind and temperature. Therefore, a good understanding of the atmosphere and its wave propagation is necessary to interpret the infrasonic events (Bedard & Georges, 2000).

1-2 Source mechanisms

Infrasound is generated by significant pressure variations in the atmosphere, i.e., when a large volume of air is disturbed. Therefore, sources of infrasound are vast and powerful (Evers, 2008). The different infrasonic sources are distinguished by recognising the particular frequency-versus-time signature of the sound, the direction and duration of the signal. The characteristics of infrasound sources are shown in Table 1-1. Some sources of infrasound will be described, but there are many other sources. Examples with real-life data can be found in Campus (2004).

The first example of infrasound source is avalanches. It is identified by its train of nearly monochromatic waves (i.e., waves with a single frequency). Infrasound originates from the displacement of large volumes of snow and ice. When avalanches are moving faster, it generates lower frequencies, and the infrasound waves can, therefore, travel longer distances. The purpose of monitoring infrasound of avalanches is a short-term warning for avalanches and collecting avalanche statistics (Ulivieri et al., 2011).

A continuous background noise of atmospheric infrasound are microbaroms. The microbaroms have a typical frequency of 0.2 Hz. The infrasound waves are generated by a non-linear interaction of ocean swell with, e.g., marine storms around the world. These storms can be seen as large low-pressure systems. It is accordingly called the 'voice of the sea.' The signal of microbaroms is incoherent in space suggesting a spatially extended source.

Infrasound is further generated when a meteorite penetrates through the atmosphere. It produces natural pressure waves (like sonic booms). Nearly all meteorites burn at 30-50 km altitude in the atmosphere through a thermal explosion, which generates another infrasound wave, and this is visible on the infrasound recordings (Evers, 2008).

Earthquakes and volcanoes are likewise to produce infrasound waves. Earthquakes produce infrasound through the displacement of the earth surface over large regions. Infrasound waves appear through three mechanism due to earthquakes: **1.** by near vertical radiation of acoustic wave away from earth surface, **2.** by violent ground movement at the epicentre of a shallow earthquake, and **3.** by seismic waves of earthquakes causing motion in mountains and these

mountains emit infrasound waves (Campus & Christie, 2010). Volcanoes are a primary source of infrasound. Infrasound forms by atmospheric disruption resulting from explosive ejection of lava and gas. The size of the explosion determines the frequency and amplitude of the signal, but the waves have mostly a broad range of frequencies. An infrasonic signal of a volcano is recognised by an initially, impulsive signature followed by a long train of asymmetrical waves. Monitoring infrasound waves of shuddering volcanoes has the purpose of predicting the possible threat of volcanic eruption and ash emission for aviation (Campus & Christie, 2010).

Besides the above mentioned natural infrasound sources, there are man-made infrasound sources. An example of this are aeroplanes. Two types of aeroplane infrasound sources exist: subsonic and supersonic. Subsonic are large amplitude waves created by take-off and landing of an aeroplane, and super-sonic is a shock wave occurring when a plane travels close to the speed of sound. The infrasound wave is then a sonic boom signal in the form of N-wave pressure signature, and it can be seen as the direct arrivals of aeroplanes (Campus & Christie, 2010).

Another example of man-made infrasound source is a (chemical) explosion. The infrasound wave is characterised by a sharp onset wave. Therefore, it has been used to study the low-frequency sound propagation through the atmosphere and to acquire information about the properties of the atmosphere. Furthermore, monitoring infrasonic waves of explosions is used to derive source characteristics for forensics such as the location, time, and strength of the blast (Evers, 2008).

Table 1-1: Properties of infrasonic waves by Campus & Christie (2010)

Infrasound source	Frequency range (Hz)	Typical observed amplitude (Pa)
Avalanches	0.5 - 8	~ 1
Microbaroms	0.12 - 0.35	~ 5
Meteoroid	0.01 - 20	>10
Earthquakes	0.005 - 10	~ 4
Volcanoes	0.002 - 20	>20
Aeroplanes	0.3 - 20	~ 2 (sub), ~ 10 (super)
Chemical explosion	0.05 - 20	~ 10

1-3 Earlier research

Several authors in the literature have already addressed the analysis of infrasound caused by an explosion. Most authors have used the clear signal of the explosion to investigate the atmosphere at different locations in the world. In this section, the critical articles concerning this topic will be reviewed.

One of the first observations of infrasound from explosive source was in 1917 due to the explosion of a munitions factory in East-London. Davison (1917) used the explosion to gain knowledge about the propagation of sound waves through the atmosphere. He concluded that there existed zones of silence, which separate areas where the sound is audible. He could not explain it yet, except giving a theory of refraction of sound waves by the wind.

Some year later, the zone of silence due to wind and temperature variations is further questioned in Nature (1922). An experiment was conducted by letting the Ministry of War perform an explosion. The infrasound was traced while attention was paid to the meteorological conditions at the moment of explosion. The results of the experiment were unfortunately not shown in the article as the name of the author.

Wexler & Hass (1962) continue with increasing the understanding of the atmosphere by infrasound from explosions. They investigated the infrasound set off by the Soviet nuclear test on October 30, 1961. These infrasound waves were traced over the whole world. The global geographic variations in propagation speed and amplitude as a function of air density and wind analysis were observed. Probably not all observations were real, but the influence of wind and temperature was noticeable. In addition, Donn & Ewing (1962) examined the same explosion on October 30, 1961, at nine stations having a global distribution. They showed that the atmospheric waves travelled around the earth more than once and were influenced by global atmospheric conditions. They also concluded that all records began with a train of waves showing normal or direct dispersion.

Green et al. (2011) state that due to the complexity of the atmosphere, it is sometimes difficult to correlate the observed infrasound with the velocity profiles from meteorological observations. They analysed unexpected arrivals from two series of accidental weapon dump explosions in 2008 and concluded that gravity waves induced horizontal wind fluctuations have a significant influence on the returning of sound waves back to the Earth's surface.

The fact that temperature and the wind affect the propagation of the sound waves through the atmosphere is identified, and Marcillo et al. (2014) used blast waves from a chemical explosion to provide information on changes in temperature and wind around the time of the explosions. It was possible through repetitive nature of the explosion, and the coda delays were modelled as changes in velocity due to temperature changes.

In Ceranna et al. (2009), different propagation algorithms and atmospheric models for phase identification, source location, and yield estimation are studied using the Buncefield Oil Depot explosion in 2005. The study is seen as a benchmark for infrasound analysis providing improved atmospheric models and a better understanding of the complexity of the atmosphere.

Gitterman & Hofstetter (2014) state that infrasound stations should be calibrated to improve monitoring explosive sources. So they used fully-controlled infrasound sources containing ground-truth-zero (GT0) information for calibration of the International Monitoring System (IMS). They produced the first GT0 infrasound data set for the IMS, and this data set provides valuable information for infrasound propagation modelling. More calibration experiments were performed in Fee et al. (2013) to test the IMS network. They executed different explosions at various times in the year to compare events under different atmosphere conditions. It was shown that infrasound could travel over long distances trapped in ducts created by atmospheric wind and temperature, and illustrated that calibration experiments are needed to get a better understanding of the atmosphere.

To ensure the correctness of the infrasound data, infrasound data and seismic data can be correlated for monitoring or verification as mentioned in Evers (2008). Furthermore, as explosions created both infrasound and seismic data, the combination can be used in the forensic investigation to better resolve time, location and strength of the explosion. Likewise, Gibbons & Ringdal (2010) analyse seismic and infrasonic signals of near-surface explosions on the

Kola Peninsula. They revealed that the best seismic location estimate coincides with the back azimuth of the infrasound data. Moreover, they concluded that acoustic signals are observed at greater distances than seismic signals and that stratospheric winds mostly control these infrasound signals.

One of the most recent developments is the detection of infrasound from underground nuclear explosions published in Assink et al. (2016). They analysed the underground nuclear test by the Democratic People's Republic of Korea (DPRK) in 2013 and 2016. The infrasound signal in 2016 was much weaker while the seismic signal was the same. They hypothesise that the test in 2016 was 1.5 times deeper than in 2013. Depth estimation is difficult with seismics alone, but the combination with infrasound opens a new application of seismo-acoustic observations.

1-4 Study objectives

The objective is to obtain knowledge of the 3D infrasonic wavefield and the waveform coherency in the atmosphere by analysing a particular event: the explosions at Shell Moerdijk in 2014. In the Netherlands, a unique three-dimensional (3D) infrasonic array, the Cabauw Infrasonic Array (CIA), is situated. This array is the property of the Royal Netherlands Meteorological Institute (KNMI). The CIA contains ten ground sensors and five sensors in the meteorological tower. These tower sensors reach a height up to 200 meters. By combining the infrasound data with the meteorological data from the tower, the study of the wavefront coherency in the atmosphere can be conducted. Moreover, due to the 3D measurements of the infrasound, the signature of the waveform as a function of altitude can be studied to understand the 3D infrasound wavefield. Therefore, the central research question is: what is the added value of measuring infrasound in 3D ? The Shell Moerdijk explosions are used to answer this question. The answer will be given in the conclusion. This research contributes to the use of infrasound as a verification technique for the Comprehensive Nuclear-Test-Ban Treaty (CTBT, www.ctbto.org). In addition, this study gives a detailed description of the processing steps, yield determination, and atmospheric wave propagation.

1-5 Outline of the thesis

After the introduction with the problem description, this thesis will have the following outline. Chapter 2 describes the theory of the measurements and array processing. The instrument for infrasound detection is illustrated as well as the array response and design. Furthermore, the applied array processing techniques for detecting signals of interest, called the Fisher analysis, is described. Additionally, the array processing in 2D and 3D are given. Moreover, the general characteristics of the atmosphere, the effective velocity in the atmosphere and the theory of ray tracing are explained. Finally, chapter 2 contains the principles of estimating the yield of an explosion.

Chapter 3 includes the case study of the Shell Moerdijk explosions. It gives background information on the explosions of Shell Moerdijk in 2014, and it shows the result of the time domain and frequency domain Fisher analysis in 2D and 3D. Additionally, the tower signals are investigated in more detail, and the results of the yield estimation are given.

In chapter 4, the observed infrasound waves caused by the Shell Moerdijk explosions are explained by atmospheric propagation modelling. It includes the results from ray tracing based on the meteorological data. Chapter 5 contains the evaluation of the Shell Moerdijk explosions. The results are interpreted to obtain knowledge of the 3D infrasonic wavefield. Moreover, a small summary of the case study is given.

The final chapter, chapter 6, contains the discussion and the conclusion. It includes summing the main findings and addressing the objectives of the research. Moreover, the possible topics for further research are addressed.

Chapter 2

Theory about measurements/processing, propagation and the yield

This chapter describes the theory behind the array processing. Furthermore, the measurement of infrasound is described. The chapter is divided into three sections; the infrasound arrays including the array processing in two-dimensional (2D) and in three-dimensional (3D), the propagation and the yield estimation.

2-1 Infrasound arrays

2-1-1 Instrumentation

The KNMI microbarometer measures infrasound. It is a very sensitive barometer able to detect small air pressure fluctuations in the order of 10^{-2} Pa. The atmosphere is sampled with a minimum of 40 Hz. The microbarometer measures the pressure difference between the infrasonic pressure and the reference pressure in the backing volume, see figure 2-1. The atmosphere is sampled through aluminium pipes on top of the sensor (i.e., the inlet box) to which a pressure sensor is attached. The backing volume is connected to this pressure sensor which measures the whole frequency range of atmospheric fluctuations (Evers, 2008). A low-frequency cut-off is accomplished by a leak in the backing volume. This leak consists of a thin capillary that acts as an acoustic resistance. Fluctuations with too large periods are transformed back to the atmosphere. Due to this acoustic resistance, the capillary controls the low-frequency cut-off, which is 500 seconds, by its length and diameter. The size of the backing volume also regulates the low-frequency cut-off (Evers et al., 2000).

The KNMI microbarometer is placed underneath the Earth's surface, in a watertight PVC tube, to avoid temperature fluctuations. The microbarometer is even more protected by placing Styrofoam plates in the tube and by adding a concrete cover. Furthermore, infrasound

is very sensitive to the wind noise, especially in the frequency range of 1-10 Hz. The effect of wind can be reduced by averaging the pressure field over an area instead of measuring it at a single point. It is achieved by sampling atmosphere with porous hoses. This analogue filter is applied to improve the signal-to-noise ratio (snr). However, the infrasound data of the microbarometers can be corrupted if the connection of the microbarometer with the server is lost, the hoses are broken or have bite marks due to the animals in the field, or if the microbarometers are filled with water through rainfall or groundwater breakthrough. Therefore, before processing, the raw data of every microbarometer needs to be checked and judge on its quality. Infrasound is measured with multiple microbarometers close together, called an array. For a more detailed description of the instrumentation, see Evers (2008).

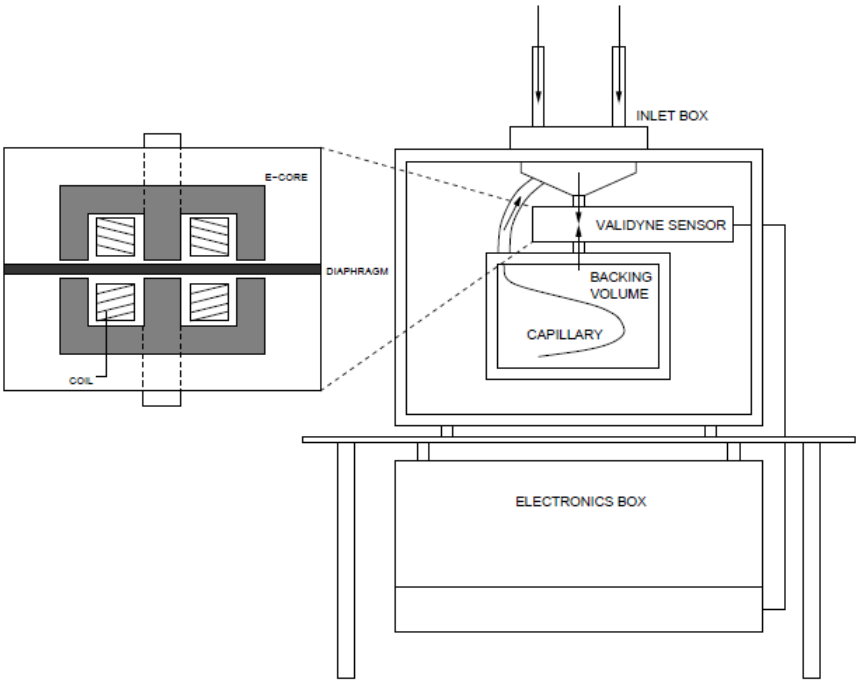

Figure 2-1: The KNMI microbarometer, schematic overview. An array consist of multiple of these microbarometers. Figure taken from Evers (2008).

The microbarometers in the meteorological tower in Cabauw are the same instruments, but they are without porous hoses. These microbarometers are placed on their side attached to the inside of the tower with a small opening to the outside connected to the atmosphere. The small opening is working as a filter for wind noise, and therefore, no porous hoses are needed.

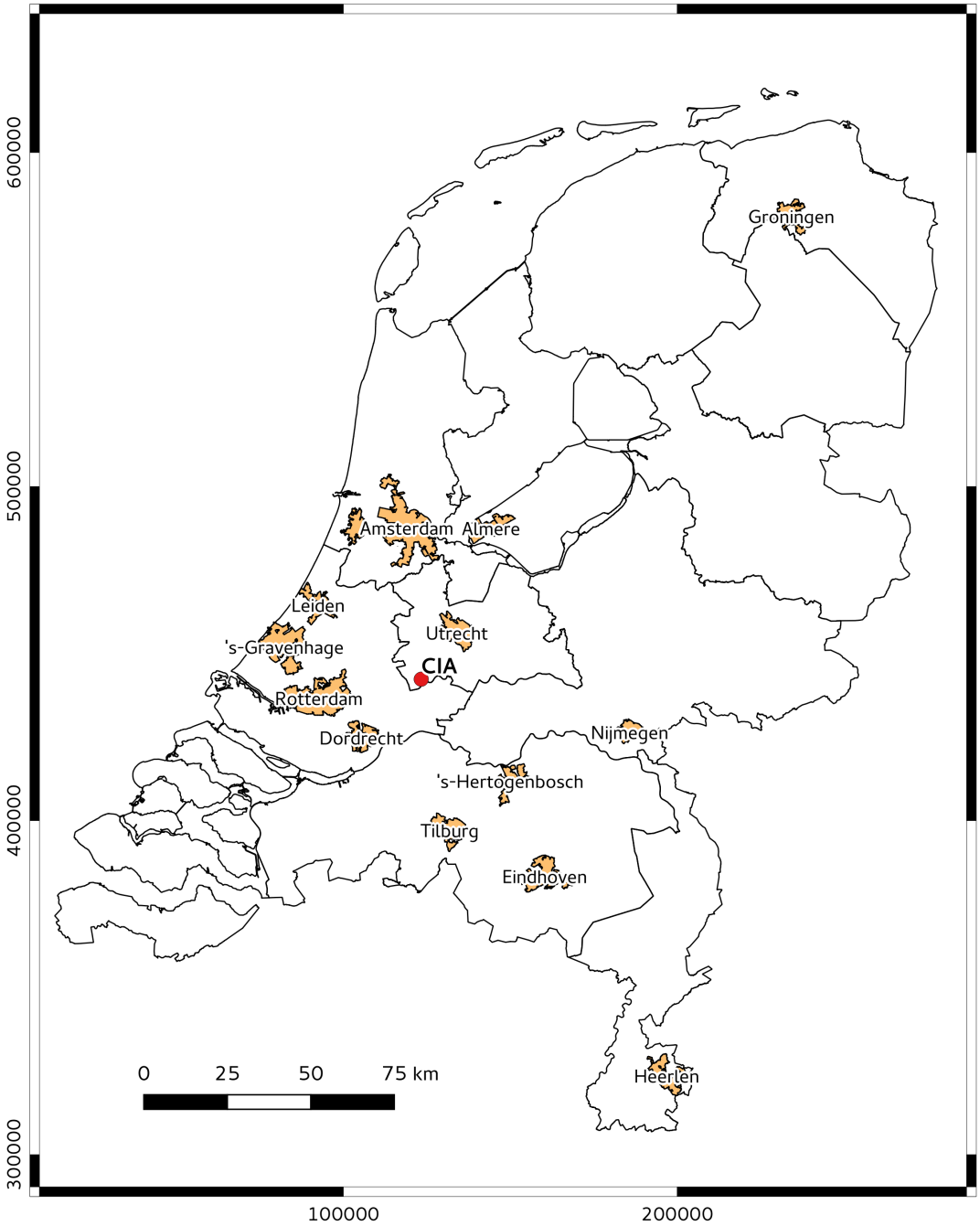

Figure 2-2: The location in the Netherlands of the KNMI Cabauw Infrasound array (CIA) in RD coordinate system

2-1-2 Array response and design

The array can detect the signal and the direction of the energy by its design. The array used in this study is the Cabauw infrasound array (CIA) from the KNMI situated in the Netherlands, see figure 2-2. The array increases the snr by signal summation with $1/\sqrt{N}$ where N is the number of microbarometers (or sensors or elements) in the array. The array discretely samples the wavefield of the signal, where the spatial sampling is controlled by the number of sensors in the array and the temporal sampling by the sample rate Δ. A plane wave is assumed and described by, see Assink et al. (2008):

$$g(t, \vec{r}) = e^{i(\omega_0 t - \vec{k}_0 \cdot \vec{r})} \tag{2-1}$$

where angular frequency ω_0, travel time t, wavenumber $\vec{k}_0$ at position $\vec{r} = (x, y, z)$. The Fourier transform of the signal is defined as in Evers (2008):

$$G(\omega; \vec{r}) = \int_{-\infty}^{+\infty} g(t, \vec{r}) e^{-i\omega t}\, dt = \delta(f - f_0) e^{-i\vec{k}_0 \cdot \vec{r}} \tag{2-2}$$

The output of the array for a signal with a different wavenumber, using equation 2-1, can be written as:

$$y(t; \vec{r}) = \frac{1}{N} \sum_{n=1}^{N} e^{i(\omega_0 t + (\vec{k}_0 - \vec{k}) \cdot \vec{r})} \tag{2-3}$$

The amplitude of the sum of all sensors has its maximum when the time shift $\vec{k}_0 \cdot \vec{r}$ has disappeared. Therefore, the output of the array has a + sign in the equation. The total energy registered in the array can be calculated of the squared summed amplitudes over time (Rost & Thomas, 2002):

$$E(\vec{k} - \vec{k}_0) = \int_{-\infty}^{+\infty} |\, y(t, \vec{r})|^2\, dt \tag{2-4}$$

Using Parseval's theorem which states that integral of squared function is equal to integral of the square of its transform, equation 2-4 in the f/k-spectrum can be rewritten as:

$$E(\vec{k} - \vec{k}_0) = \int_{-\infty}^{+\infty} |\, y(t; \vec{r})|^2\, dt = \int_{-\infty}^{+\infty} |\, Y(\omega; \vec{r})|^2\, df \tag{2-5}$$

$$= \int_{-\infty}^{+\infty} |G(\omega)|^2 \left| \frac{1}{N} \sum_{n=1}^{N} e^{-i[(\vec{k} - \vec{k}_0) \cdot \vec{r}_n]} \right|^2 df \tag{2-6}$$

where $|G(\omega)|$ is the Fourier transform of $g(t)$ without a time shift $\vec{k} \cdot \vec{r}$. The array response is written as:

$$R(\omega;\vec{p}) = \left| \frac{1}{N} \sum_{n=1}^{N} e^{-i\omega[(\vec{p}-\vec{p}_0)\cdot\vec{r}_n]} \right|^2 \tag{2-7}$$

where $\vec{p}_0 = \frac{1}{\omega}(k_{0x}, k_{0y})$ is the slowness vector and $\vec{r}_n$ the location positions normalised by subtracting the mean of the positions. The total energy in equation 2-6 consist of the array response and the power spectral density $|G(\omega)|^2$.

The array response can be plotted by choosing a particular frequency and slowness grid. The array response of the ground elements of CIA is shown in figure 2-3 for different frequencies and array designs. The red colour indicates for which elements the array response is calculated. The last column contains the array layout and response for all sensors of CIA. The number of sensors and inter-sensor distances controls the resolution and is limited by spatial aliasing. Aliasing is the effect when a signal can not be uniquely resolved. The Nyquist frequency is defined as $f_N = \frac{1}{2\Delta t}$ and forms the upper-frequency limit. The diameter of the array controls the lower frequency limit.

An optimal array is uniformly sensitive to all infrasonic signal regardless the direction of arrival. This is shown in the array response as a circular lobe in the middle at $p_x = p_y = 0$, seen in the first two columns in figure 2-3, (Evers et al., 2000). However, the location of the elements, as well as the distance between the elements, influences the array response. This can be seen when comparing column one and three of figure 2-3. When the array response is stretched in a particular direction, the array is less sensitive to detect a signal in that direction as shown in the third and fourth column of figure 2-3. Moreover, by increasing the number of elements, the snr is increased. The Matlab script for the array design is added in appendix A-1.

2-1-3 Beamforming

An array is designed to detect a wave and to estimate the wave's orientation and velocity for identifying the source location or for snr improvement. It is achieved by the fact that the wave propagates through the medium with a finite velocity and therefore is detected by each sensor at different times, Δt. The time delay is related to the receiver position, $\vec{r} = (r_x, r_y, r_z)$, compared to a reference location (for example, compared to the mean of the location), and the wave direction $\vec{p}$. Furthermore, it depends on the propagation direction and velocity of the wavefront. The relative time delay is defined as:

$$\Delta t = -(\vec{r}\cdot\vec{p}) = -(r_x p_x + r_y p_y + r_z p_z) \tag{2-8}$$

under the assumption of planar wave approximation. The negative sign in equation 2-8 is inserted to give the direction of the slowness vector where the wave originates with respect to the receiver. Beamforming is steering the array sensitivity in a certain direction. In theory, a search is performed over a slowness grid to explain the observed time delay. Beamforming is mostly applied only to the horizontal plane to reduce the computation grid search expenses (Edwards & Green, 2012). Here the assumption is made that the vertical component of the time delay is much smaller than the horizontal component of the time delay:

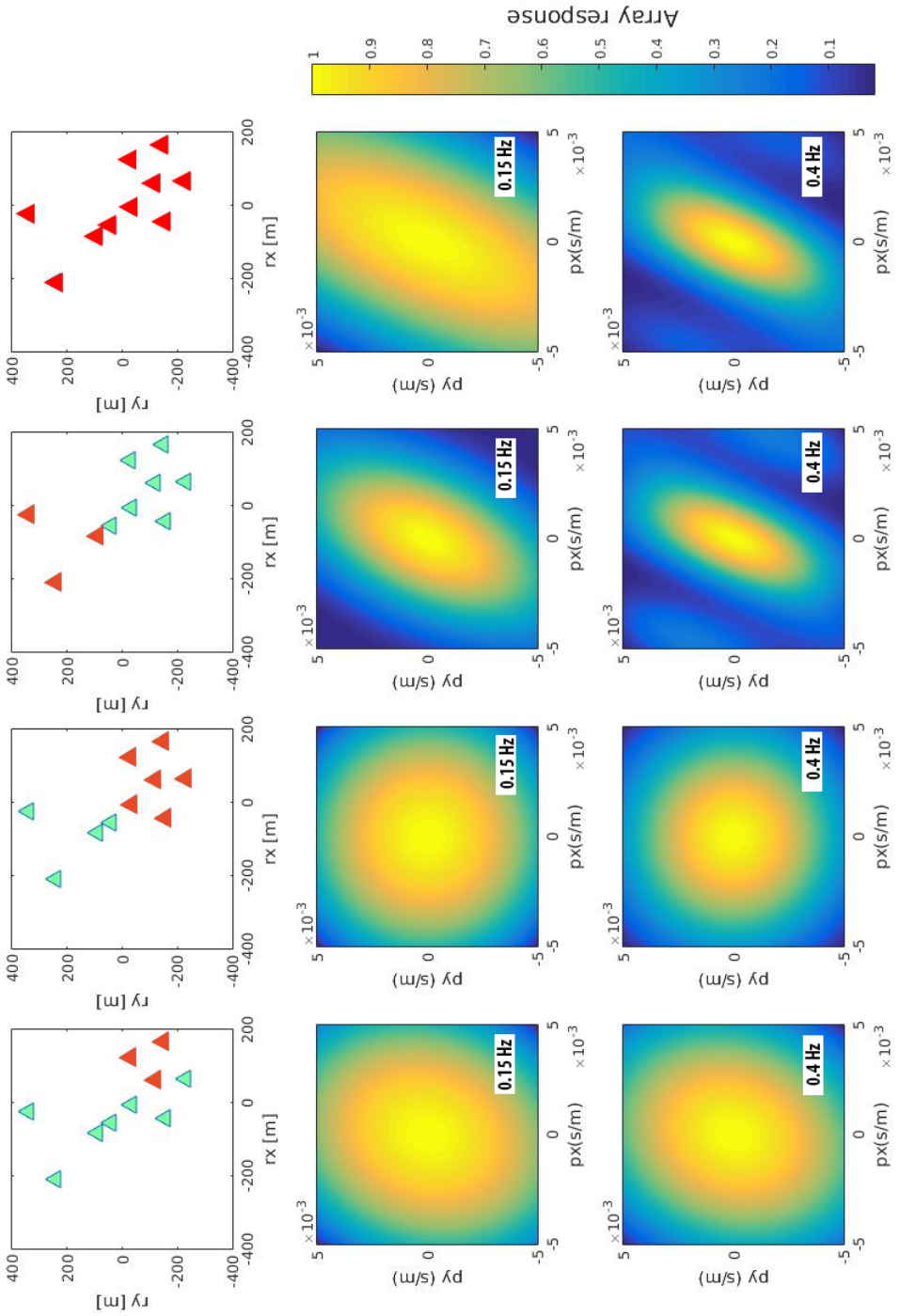

Figure 2-3: The columns show the array response and their layout for the CIA choosing a different number of elements and their location. The fourth column shows the array layout and response from all elements in the CIA. The red colour indicates the elements for which the array response is calculated. In the lower two rows, the array response for 0.15 Hz and 0.4 Hz are plotted. If column one and three are compared, it can be seen that the location of the sensors, as well as the inter-sensor distance, influences the array response if the number of sensors is kept the same.

$$|r_z p_z| \ll |r_x p_x + r_y p_y| \tag{2-9}$$

This reduces the problem from 3D to 2D, and the assumption for the planar horizontal array is made where $r_z = 0$. As a consequence, the apparent velocity is sufficient to solve p_z.

2-1-4 Fisher analysis (coherency)

The Fisher analysis is used to process the infrasound signals. The Fisher analysis is the analysis of statistics based on the measurement of coherent signals. The signals are the waveforms at the different array elements. The algorithm estimates characteristics of a specific event by making use of a set time segments (i.e., the bins). Phrasing differently, a sample of the waveform is examined to discover the amount of coherent structure. The Fisher detection algorithm, expressed as F-ratio, is differently defined for time and frequency domain, and shows the correlation between different signals (Melton & Bailey, 1957). The time and frequency analysis are related as the Fourier transform of the time analysis is the same as the frequency analysis. The slowness vector $\vec{p}$ corresponding to the maximum Fisher value best explains the observed time delays. This slowness vector is used to construct the bestbeam. The forming of the bestbeam corresponds to stacking of the time aligned signals (Assink et al., 2008).

Time domain Fisher analysis

The time domain Fisher analysis is defined as the analysis of variance in Melton & Bailey (1957) and is used to identify a coherent signal over an array of sensors. The strength of the Fisher analysis is the constructive stacking of the signal and the nonconstructive stacking of noise (Assink et al., 2008). The data of the sensors are arranged in a matrix where the rows represent the number of sensors (N) and the columns individual time segments, also called bins (T), forming a $N \times T$-matrix. The data value at each location in the matrix is analysed (Olson, 2004). The mean of each column is defined as:

$$\bar{x}_t = \frac{1}{N} \sum_{n=1}^{N} x_{nt} \tag{2-10}$$

where x_{nt} are the time-shifted recordings of each sensor to become phase aligned. When summed over all time segments (T), the signal is enhanced with N, while the noise is enhanced with $\sqrt{N}$. The analysis uses the fact that the value at each location differs from the mean of the column by error ϵ_{nt} as $x_{nt} = \bar{x}_t + \epsilon_{nt}$ and this mean differs from the grand average of the whole matrix by $\alpha_t = \bar{x}_t - \bar{x}$. $\bar{x}$ is the grand average, or the mean of all samples, and is defined by Evers (2008):

$$\bar{x} = \frac{1}{NT} \sum_{t=1}^{T} \sum_{n=1}^{N} x_{nt} \tag{2-11}$$

To define the F-ratio, the total variance of the recordings is studied and this is expressed as $V_T = \sum_{t=1}^{T} \sum_{n=1}^{N} (x_{nt} - \bar{x})^2$ or with some mathematics as

$$V = V_W + V_B \tag{2-12}$$

with

$$V_W = \sum_{t=1}^{T}\sum_{n=1}^{N}(x_{nt} - \bar{x}_t)^2 \tag{2-13}$$

and

$$V_B = N\sum_{t=1}^{T}(\bar{x}_t - \bar{x})^2 \tag{2-14}$$

V_W can be seen as the variance containing both signal and noise, while V_B includes only the signal power. The ratio V_B/V_W is equal to the snr^2. V_W stands for the variance within a recording as it investigates each location with the mean of each column. V_B stands for the variance between the recordings as it compares the mean of each column with the grand average. The total variance V_T is split into two components to test the amount of variance in one variable is explained by the other one. Combining the equations mentioned above, the F-ratio is defined as:

$$F = \frac{V_B/(T-1)}{V_W/T(N-1)} \tag{2-15}$$

or as expressed in Melton & Bailey (1957):

$$F = \frac{T(N-1)}{N(T-1)} \frac{\sum_{t=1}^{T}(\sum_{n=1}^{N} x_{nt})^2 - \frac{1}{T}(\sum_{t=1}^{T}\sum_{n=1}^{N} x_{nt})^2}{\sum_{t=1}^{T}\sum_{n=1}^{N} x_{nt}^2 - \frac{1}{N}\sum_{t=1}^{T}(\sum_{n=1}^{N} x_{nt})^2} \tag{2-16}$$

Melton & Bailey (1957) also derived a relationship between the signal-to-noise power ratio (snr^2) and the F-ratio. This relationship is very important as it gives the snr^2 required for detection and can be written as:

$$snr^2 = \frac{1}{N}(F-1) \tag{2-17}$$

As an example of the time domain Fisher analysis in 2D, the data from the DIA array described in chapter 2 of Evers (2008) are taken. Thirteen of sixteen sensors in this array were active at the moment of measuring. In figure 2-4 the data from the DIA array on 2007, September 04 at 20h03m18.475s UTC is shown. The data have been bandpass filtered between 0.1 and 5 Hz. The upper panel shows the raw data, and the lower panel shows the phase aligned data. The arrivals between 140 and 150 s show the highest amplitude.

In figure 2-5, the results of the time domain Fisher analysis is visualised. The recordings are split in 50% overlapping bins of 512 samples with a sample rate of 0.025 seconds. Within each bin, a slowness grid search of 50×50 is performed, and the maximum F-ratio is plotted. The bestbeam is constructed with the slowness vector at the maximum F-ratio. The maximum

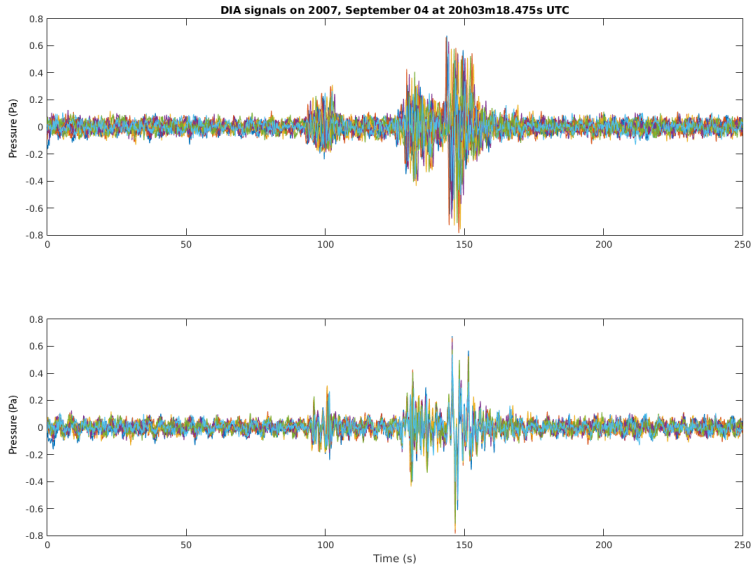

Figure 2-4: The raw (top frame) and the phase aligned (lower frame) data from the DIA array filtered between 0.1 and 5 Hz.

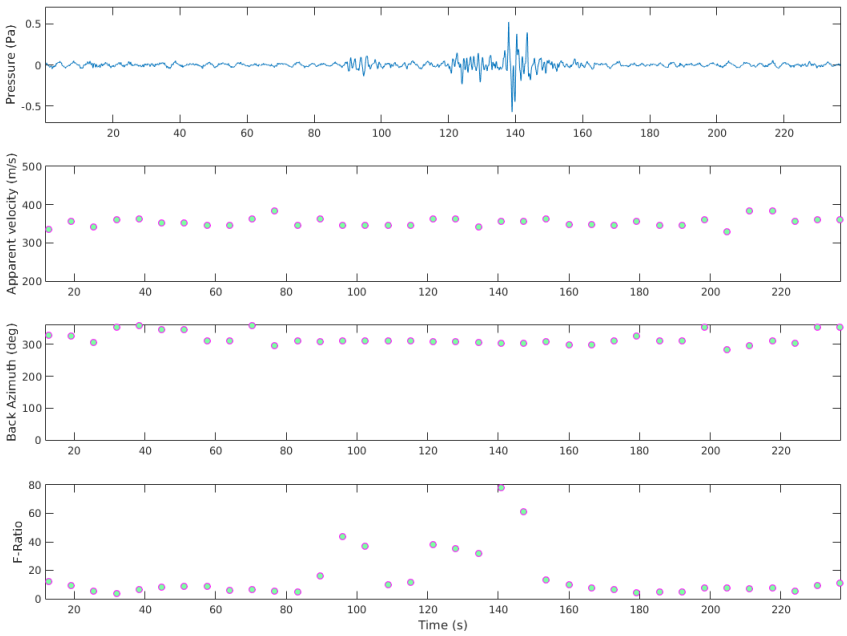

Figure 2-5: The 2D time domain Fisher Analysis from the DIA array on 2007, September 04. From top to bottom, the figure shows the bestbeam, the apparent velocity in m/s, the back azimuth in degrees and the F-ratio.

F-ratio of 78 is found around ∼140 seconds. The resolved back azimuth is 303.1° and the apparent velocity is 356.9 m/s.

The time domain Fisher analysis performs well when the snr is high but is challenged when there are multiple signals present in the data with different frequencies. Then, a signal can be missed. In that case, the frequency domain analysis would perform better. However, an advantage of the time domain analysis is that it is more stable than the frequency domain.

Frequency domain Fisher analysis

The frequency domain Fisher analysis is described in Smart & Flinn (1971) as the Fisher statistics based on the frequency-wavenumber (f/k) spectrum. Instead of the time domain analysis, it takes the frequency variations of the signal's back azimuth and apparent velocity into account by computing the power spectral density from the data (Olson, 2004). The Fisher values are a measure of signal coherency and are extracted for each frequency and each beam as a function of apparent velocity and back azimuth. Signals have a high Fisher value, while noise has a small Fisher value (Evers et al., 2000).

The advantage of this F-statistics is that it can separate different propagating waves if the frequency contents differ. It is, therefore, a powerful tool for signal detection and waveform analysis (Assink et al., 2008). By estimating the apparent velocity and back azimuth from frequency to frequency, this method is more sensitive than computing broadband beamforming (as in the time domain). Furthermore, the snr is higher when the signal characteristics are calculated over one frequency at a time or a small frequency band. The computation time of the F-ratio is reduced by limiting the frequency band of interest as it is often not necessary to go up to the Nyquist frequency. The F-ratio is the ratio of the power at a particular point in the f/k-domain, and the difference between that power and the total power in the recordings weighted by the sensors as defined in Evers (2008). It is based on snr^2 in equation 2-17:

$$F(\omega, \vec{k}) = \frac{P_S(\omega, \vec{k})}{P_T(\omega) - P_S(\omega, \vec{k})}(N-1) \tag{2-18}$$

where

$$P_T(\omega) = \frac{1}{N}\sum_{n=1}^{N} |G(\omega, \vec{r}_n)|^2 \tag{2-19}$$

is the total amount of energy including both noise and signal, and

$$P_S(\omega, \vec{k}) = \left| \frac{1}{N}\sum_{n=1}^{N} G(\omega, \vec{r}_n) e^{-i\vec{k}\cdot\vec{r}_n} \right|^2 \tag{2-20}$$

is the signal power. The denominator of the F-ratio in equation 2-18 is the noise as it is the total power minus the signal power.

The F-ratio is again searched over a slowness grid in successive time windows (these 'bins' can overlap). The Fisher spectrum is constructed in the f/k-space of interest. In this spectrum,

the highest F-ratio in each frequency slice is searched where each maximum represents a possible signal detection. From the location of the maximum F-ratio, the apparent velocity and back azimuth are constructed as well as the slowness vector (Smart & Flinn, 1971).

As an example of the frequency domain Fisher analysis in 2D, the same data from the DIA array as in the time domain analysis is taken. The data is filtered between 0.1 and 5 Hz. Figure 2-6 shows the result of the frequency domain analysis. The frequency and time axis are the same for the lower three panels, but in each panel, the third parameter is plotted like F-ratio, back azimuth and the apparent velocity. The bestbeam in the upper panel is as in the time domain the sum of all time-aligned signals and computed with the slowness vector at the maximum F-ratio.

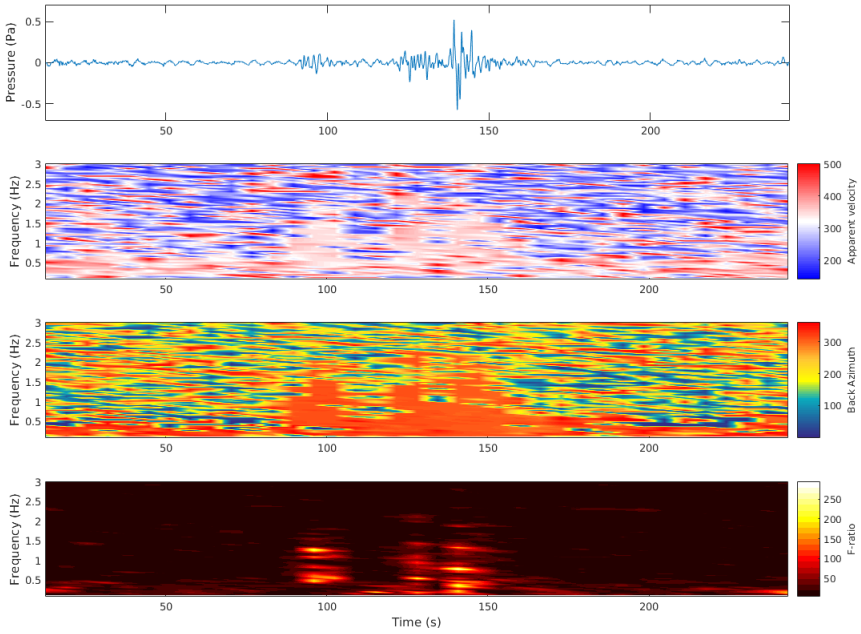

Figure 2-6: The 2D frequency domain Fisher Analysis from the DIA array on 2007, September 04. From top to bottom, the best beam, the apparent velocity in m/s, the back azimuth in degrees and the F-ratio are plotted.

The maximum F-ratio of 293 is found around ∼140 second corresponding to a back azimuth of 303.1° and an apparent velocity of 356.9 m/s at ∼1.3 Hz. The data is split in 50% overlapping bins with a binsize of 512 samples. There is a difference between the F-ratio of the time and frequency domain analysis because in the frequency domain each frequency is analysed individually and thus gives a higher F-ratio value.

Several signals are detected in the frequency domain Fisher analysis at different frequencies. This analysis displays every event as it occurs in the frequency-time space for all slowness values. It is therefore more accurate in detecting multiple signals when the frequencies differ.

2-1-5 2D array processing

The 2D array processing uses the 2D slowness vector $\vec{p} = (p_x, p_y)$ to resolve the back azimuth and apparent velocity. These parameters are solved for each bin with a slowness vector corresponding to the maximum Fisher value of that bin. The back azimuth, ϕ, and apparent velocity, c_{app}, are solved by:

$$\tan \phi = \frac{p_x}{p_y} \tag{2-21}$$

The back azimuth ϕ is the angle between the receiver and the source in the xy-plane measured clockwise. The apparent velocity is defined as:

$$c_{app} = \frac{1}{\sqrt{p_x^2 + p_y^2}} \tag{2-22}$$

The apparent velocity can also be related to the effective velocity c_{eff} through the incidence angle by $c_{app} = \frac{c_{eff}}{\cos \theta}$. The effective velocity takes the temperature and the wind into account as a force affecting the wave propagation speed in the xyz-plane (Evers, 2008), see section 2-2-2 for a more detailed description of the effective velocity. An estimate of the incidence angle can be made with the measured apparent velocity and the local temperature at the Earth's surface (i.e., the effective velocity only becomes a function of temperature as the wind has a velocity of 0 m/s at the surface). Errors in back azimuth and apparent velocity occur when the inclination becomes more vertical and assumption 2-9 is no longer valid. A solution for this problem is performing a grid search of slowness space in 3D to find the orientation of the slowness vector. Through this 3D grid search, a more accurate understanding of the wave propagation through the atmosphere can be obtained. This will be further described further in the next section.

2-1-6 3D array processing

To prevent the error of the 2D approximation in equation 2-9 for inclined arrays or arrays with significant topography, a 3D grid search of the slowness vector is performed to determine the slowness vector $\vec{p}$. All possible orientations (the back azimuth ϕ and the vertical incidence angle i), and the magnitude of the slowness vector are investigated. The vertical incidence angle is measured from the vertical to the direction of propagation (Rost & Thomas, 2002). The vertical incidence angle can be negative as it is measured anticlockwise from the vertical. The 3D grid search is limited by the effective velocity c_{eff}, and the amount of coherency. The effective velocity c_{eff} is defined in detail in section 2-2. Instead of search over the slowness plane (p_x, p_y), it becomes a search over volume (p_x, p_y, p_z) defined by Edwards & Green (2012) as:

$$p_x = \frac{\sin \phi \sin i}{c_{eff}} \tag{2-23}$$

$$p_y = \frac{\cos \phi \sin i}{c_{eff}} \tag{2-24}$$

$$p_z = \frac{\cos i}{c_{eff}} \tag{2-25}$$

The main difference with 2D array processing is that $r_z \neq 0$. In figure 2-7, the 3D slowness vector is visualised in the z, y-plane. The vertically placed microbarometers represents the meteorological tower. The apparent velocity is related to the vertical incidence angle by:

$$c_{app} = \frac{1}{\sqrt{(p_x^2 + p_y^2)}} = \frac{c_{eff}}{\sin i} \tag{2-26}$$

The vertical apparent velocity is given by $c_{app-vertical} = 1/p_z$ and the vertical incidence angle can be calculated by:

$$\tan i = \frac{1}{p_z \cdot c_{app}} \tag{2-27}$$

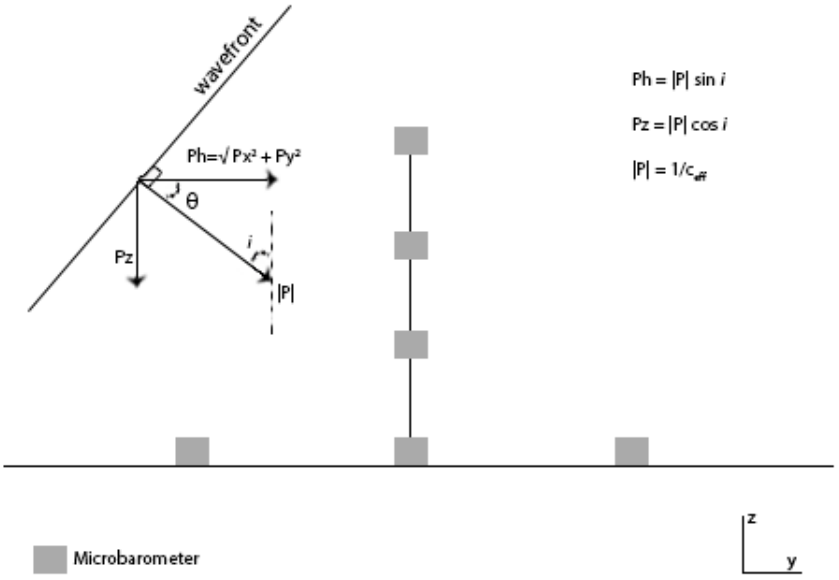

Figure 2-7: Schematic image of 3D slowness grid. It shows the wavefront approaching the meteorological tower.

2-2 Propagation

In this section, the general characteristics of the atmosphere is given as well as theory of the effective velocity in the atmosphere. This section ends with the theory of acoustic propagation modelling also known as ray tracing.

2-2-1 General atmospheric characteristics

The atmosphere consist of different layers based on the sign of the temperature gradient. This is shown in figure 2-8. The lowest layer (below 10 km) is the troposphere where temperature decreases with a lapse rate of -6.5 °C/km. In reality, a temperature inversion (i.e., temperature increases with altitude) can occur from the first 100 m to several km (Evers & Haak, 2010). The troposphere is followed by the tropopause (10-17 km) where the temperature is constant. The tropopause indicates the transition into the stratosphere where the temperature increases with altitude up to the stratopause (45-55 km). This is due to the presence of ozone which absorbs the ultraviolet radiation. After the stratopause, the temperature decreases with height in mesosphere until the mesopause is reached at 80-85 km. In the overlying thermosphere, the temperature increases again with height due to absorption of energetic solar radiation until 200 km.

In the absence of clouds, the temperature profile is controlled by the absorption of solar radiation. Molecular oxygen absorbs short wavelength radiation (i.e., visible light) at an altitude of 100 km. Between 35-70 km, ultraviolet radiation is absorbed by ozone and infrared radiation (i.e., invisible light) emitted by CO_2. Below 15 km, water gas and CO_2 absorb infrared radiation reflected by the Earth. Visible radiation is absorbed at ground level by land and sea surfaces (Garcés et al., 1998).

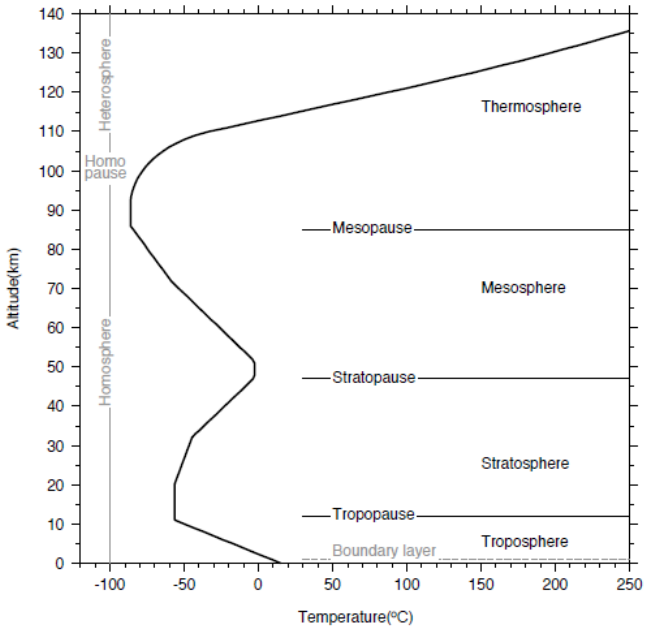

Figure 2-8: Temperature profile as function of height extracted from the U.S. Standard Atmosphere (NOAA, 1976). Positive and negative temperature gradients are separated by regions of constant temperature.

The atmosphere consists of 78% nitrogen, 21% molecular oxygen and the final 1% is water gas, CO_2, ozone and other minor components. Classical and relaxation mechanism causes the absorption of sound in a molecular gas, and it is a function of frequency. If the frequency is decreasing, the absorption of sound is declining. The classical mechanism is formed by transport processes in a gas, while relaxation mechanism is formed by compressional energy

stored in the internal dimensions of the molecules (Evers & Haak, 2010). Knowledge of the characteristics of the atmosphere is necessary for approximate acoustic propagation modelling named ray tracing. The theory of ray tracing will be explained in section 2-2-3.

2-2-2 Effective velocity

Wind and temperature structures in the atmosphere primarily determine infrasound propagation. Sound radiates upward from the ground due to decreasing temperature (or effective velocity) with height in the lower atmosphere. The upward propagation infrasound refracts back to the Earth's surface where the effective velocity is larger than the effective velocity at the surface creating a waveguide or duct (Fee et al., 2013). This is illustrated in figure 2-9 where $c_2 \geq c_1$. Acoustic ducting is the trapping of sound waves between an atmospheric layer and the ground where reflection and refraction take place. The effective velocity is given by the adiabatic velocity c, and the wind in direction of propagation. The adiabatic velocity c is defined as $\sqrt{\gamma R_c T}$. The effective velocity is described by:

$$c_{eff} = c + \text{wind} = \sqrt{\gamma R_c T} + \hat{n}_{xy} \cdot \vec{u} \tag{2-28}$$

where γ is the ratio of specific heats, R_c is the gas constant for air, T is the absolute temperature and $\hat{n}_{xy} \cdot \vec{u}$ is the wind $\vec{u}$ in the direction of propagation $\hat{n}_{xy}$. The multiplication γR_c is equal to 402.8 $m^2 s^{-2} K^{-1}$. The estimate of the effective velocity in equation 2-28 requires a minimum input of data instead of a more sophisticated relationship containing chemical composition, pressure and humidity of atmosphere (Garcés et al., 1998). The refraction of infrasound can be approximated by Snell's law:

$$n_2 = \frac{\sin i_1}{\sin i_2} = \frac{c_1}{c_2} \tag{2-29}$$

where the ratio (n) of the sines of the vertical incidence angles is equal to the ratio of the effective velocities through the media.

Infrasound propagation changes with horizontal distance and altitude, and is examined with the effective velocity ratio, c_{eff_ratio}. Acoustic ducting is predicted where $c_{eff\_ratio} > 1$. It is defined as the effective velocity depended on horizontal distance and height divided by the effective velocity at the source (Fee et al., 2013):

$$c_{eff\_ratio} = \frac{c_{eff}(r, z)}{c_{eff}(0, 0)} \tag{2-30}$$

Depending on the temperature structure, a signal can still be received at a certain distance. If there is a temperature inversion, the infrasound is trapped in a duct and can be measured at great distances from the source. Moreover, the wind can bend the infrasound back to Earth's surface or destroy the duct, and these positive wind gradients can occur at different heights. Thus, besides the direct pad of the source to the receiver, the increasing wind and/or temperature with height can bend the infrasound back to the Earth's surface. Through the time difference between the different pads, a single explosion can show multiple arrivals at the receiver (Evers, 2008).

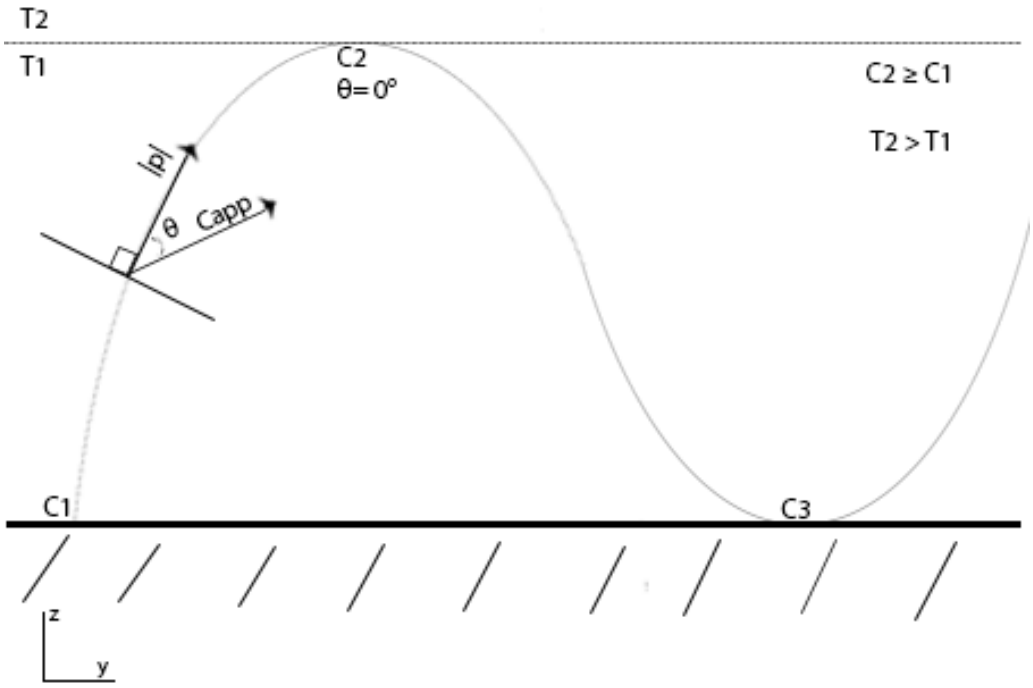

Figure 2-9: Schematic overview of ray tracing and the principle of acoustic ducting by a layer of a higher temperature. Ducting occurs where c_{eff} is larger than the c_{eff} on the surface

The horizontal wind $\vec{u}$ consists of two components: the zonal wind, which is a West-East component, and the meridional wind, which is a South-North component. An example of a profile of these winds can be seen in figure 2-10. The zonal wind is positive when blowing from the West to the East and the meridional wind is positive when blowing from the South to the North. In the winter, the zonal wind is caused by a much higher temperature gradient than in the summer which results in a stronger wind. Refractions of the sound waves are resulting from the thermosphere and stratopause where the temperature is increasing with altitude, and by the troposphere where the zonal wind is rising with altitude. The zonal (z_w) and meridional (m_w) wind are related to the wind in the direction of propagation $\hat{n}_{xy} \cdot \vec{u}$ by:

$$\hat{n}_{xy} \cdot \vec{u} = z_w \sin(\phi - 180^\circ) + m_w \cos(\phi - 180^\circ) \tag{2-31}$$

As the wind depends on the direction of wave propagation, the effective velocity profiles will change with different back azimuth. The back azimuth minus 180° is defined as the azimuth in 1D. In higher dimensions, the crosswinds have an influence and the exact difference of 180° between the back azimuth and the azimuth is no longer true.

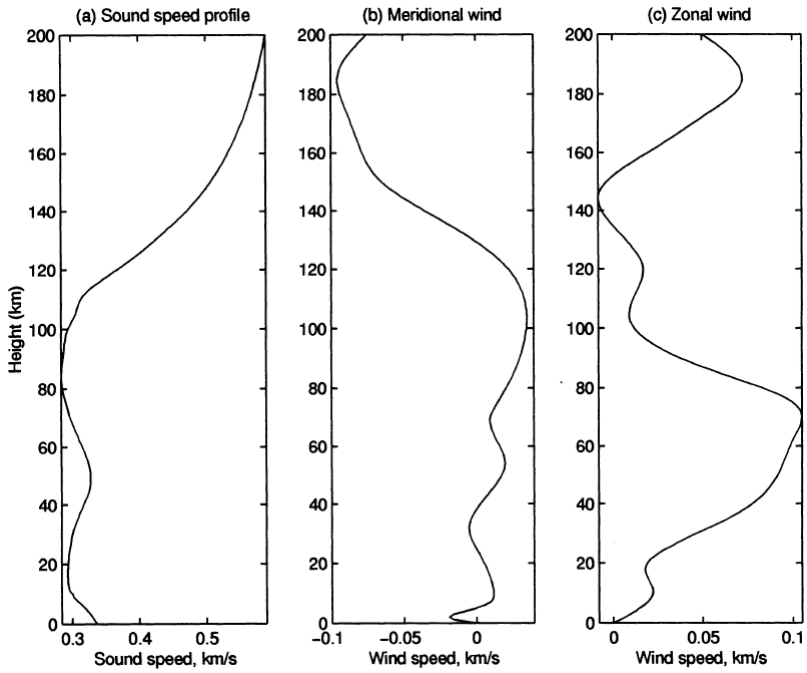

Figure 2-10: Wind profile as function of altitude extracted from Garcés et al. (1998) showing an example of a effective velocity profile, meridional wind profile and zonal wind profile.

2-2-3 Ray tracing

Ray tracing is a technique for creating an image of the rays by tracing the path of the sound waves through the atmosphere. Thus, the propagation path of infrasound in the vertical structure of the atmosphere is made visible. A ray is defined as the path which the infrasound travels. The wave equation is defined as:

$$\nabla^2\varphi(\vec{x},t) - \frac{1}{c^2}\frac{d^2\varphi(\vec{x},t)}{dt^2} = 0 \tag{2-32}$$

where $\varphi(\vec{x},t)$ is the pressure disturbance from the ambient pressure and c is the adiabatic velocity. The wave velocity is replaced with the effective velocity, earlier defined as $c_{eff} = c + \hat{n}\cdot\vec{u}$, to consider the influence of wind which gives:

$$\nabla^2\varphi(\vec{x},t) - \frac{1}{c_{eff}^2}\frac{d^2\varphi(\vec{x},t)}{dt^2} = 0 \tag{2-33}$$

The assumption of horizontal wind is made meaning no vertical winds are incoperated. A harmonic solution of the wave equation is considered in the form:

$$\varphi(\vec{x},t) = A(\vec{x})e^{-i\omega(\vec{p}(x)+t)} \tag{2-34}$$

where $\vec{p}(x)$ is the slowness vector earlier defined as $\vec{p} = \frac{\vec{k}}{\omega}$, $A(\vec{x})$ is the amplitude and $-i\omega(\vec{p}(x) + t)$ is the phase. For a plane wave (i.e., no phase shifts $\vec{p} = 0$), travel time t is equal to $\tau(\vec{x})$ which gives:

$$\varphi(\vec{x}, t) = A(\bar{x})e^{-i\omega\tau} \tag{2-35}$$

Equation 2-33 can be divided into a real and imaginary part. This is possible when the divergence of the gradient and the second derivative with respect to time of solution 2-35 is implemented back into equation 2-33:

$$\text{real} : \nabla^2 A - \omega^2 A \left|\nabla^2 \tau\right| + \frac{1}{c_{eff}^2}\omega^2 A = 0 \tag{2-36}$$

$$\text{imaginary} : i(-2\omega\nabla A\nabla\tau - \omega A\nabla^2\tau) = 0 \tag{2-37}$$

For information on propagation, only the real part must be considered and divided by $\omega^2 A$:

$$\frac{\nabla^2 A}{\omega^2 A} - \left|\nabla^2 \tau\right| = -\frac{1}{c_{eff}^2} \tag{2-38}$$

A high-frequency approximation is applied, and the limit $\omega \to \infty$ is taken. This gives the Eikonal equation:

$$\left|\nabla^2 \tau\right| = \frac{1}{c_{eff}^2} \Rightarrow |\nabla\tau(\vec{x})| = \frac{1}{c_{eff}(\vec{x})} \tag{2-39}$$

$$\nabla\tau(\vec{x}) \cong \frac{1}{c_{eff}(\vec{x})}\hat{k} = \vec{p}(\tau) \tag{2-40}$$

where $\hat{k}$ is the unit wavenumber vector for the travel time surface at position x. Thus, the gradient of a wavefront at a particular position x is equal to the local slowness vector (Lin et al., 2009). Therefore, the slowness $\vec{p}$ is perpendicular to the wavefront. Equation 2-39 is further simplified as:

$$\frac{d\tau}{ds} = \frac{1}{c_{eff}} \tag{2-41}$$

where ds stands for the distance travelled by the wave. Rewriting this to $d\tau = \frac{ds}{c_{eff}}$ which represents the travel time along ds. When a wave is travelling from point A to B, the total travel time can be written as in Jensen et al. (2011):

$$\tau = \int_A^B \frac{ds}{c_{eff}} \tag{2-42}$$

2-3 Yield of the explosion

For the comparison of two complementary explosions of different strengths and at a different altitude, atmospheric explosion waves follow the Sach's scaling laws. These laws are three simultaneous relationships (ANSI, 2011):

$$\frac{\Delta p_1}{p_1} = \frac{\Delta p_0}{p_0} \tag{2-43}$$

$$\frac{R_1}{R_0} = (\frac{W_1 p_0}{W_0 p_1})^{1/3} \tag{2-44}$$

$$\frac{t_1}{t_0} = (\frac{W_1 p_0}{W_0 p_1})^{1/3} (\frac{c_0}{c_1}) \tag{2-45}$$

Where $\Delta p/p$ is the shock strength, R is the range in km, t is the arrival time in seconds, W is the explosion energy yield in kiloton NE, and c is the adiabatic velocity in m/s. NE stands for nuclear explosions and HE for high chemical explosions. The indexes 0 and 1 are connected with the two different explosions. The Sach laws state that the shock strength of an explosion sustains with distance. At greater distances, the infrasound pressure wave of the explosion depends on the characteristics of the atmosphere and the intensity of the explosion. The signature can be disturbed by multipath propagation. The classical explosion pressure wave at a great distance is shown in figure 2-11.

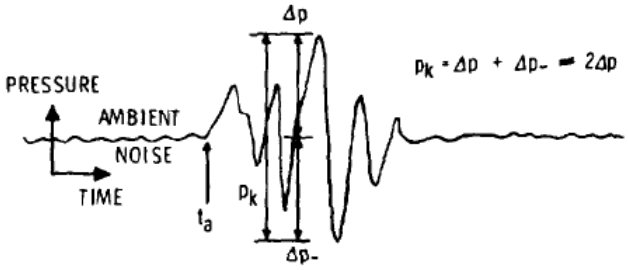

Figure 2-11: The figure shows the classic explosion wave signature at great distance taken from ANSI (2011).

For overpressure estimation, standard power laws relationships are developed for short and long distances. For distances less than 16 meters where the pressure is high, the following overpressure approximation is used:

$$1 \text{ kiloton} : \Delta p = 3.18 \times 10^5 R^{-3} \quad \text{MPa} \tag{2-46}$$

where R is distance in meters. At long distances, i.e., beyond 10 km, the following power law is derived:

$$1 \text{ kiloton} : \Delta p = 6.526 R^{-1.1} \quad \text{kPa} \tag{2-47}$$

where R is distance in km. Due to these reduced power laws, equations 2-43 and 2-44 are used to develop an equation for overpressure estimation based on yield, distance and ambient pressure described in ANSI (2011):

$$\Delta p = 6.526 W^{0.3667} R^{-1.1} (p/p_0)^{0.6333} \quad \text{kPa} \tag{2-48}$$

where W is in kilotons NE, and R in km. The parameter p/p_0 is applied when explosions take place at a certain altitude. Then, the air pressure p is lower than the air pressure at sea level p_0. The explosions from Shell Moerdijk took place at standard conditions resulting in p/p_0=1. For other yield units, different coefficients are needed as listed in table 2-1. When applying the different coefficients, explosion curves for NE and HE yield at standard conditions can be made as in figure 2-12. For the yield estimation, the measured overpressure at the array must be plotted in the figure 2-12 and the yield (or the strength) can be determined.

Table 2-1: Low pressure (kPa) equation coefficients for various yields for distance in km taken from ANSI (2011)

Yield units	**Kilometers**
metric kiloton NE (10^6 kg)	6.763
metric kiloton HE (10^6 kg)	8.720
kg NE	0.04267
kg HE	0.05309

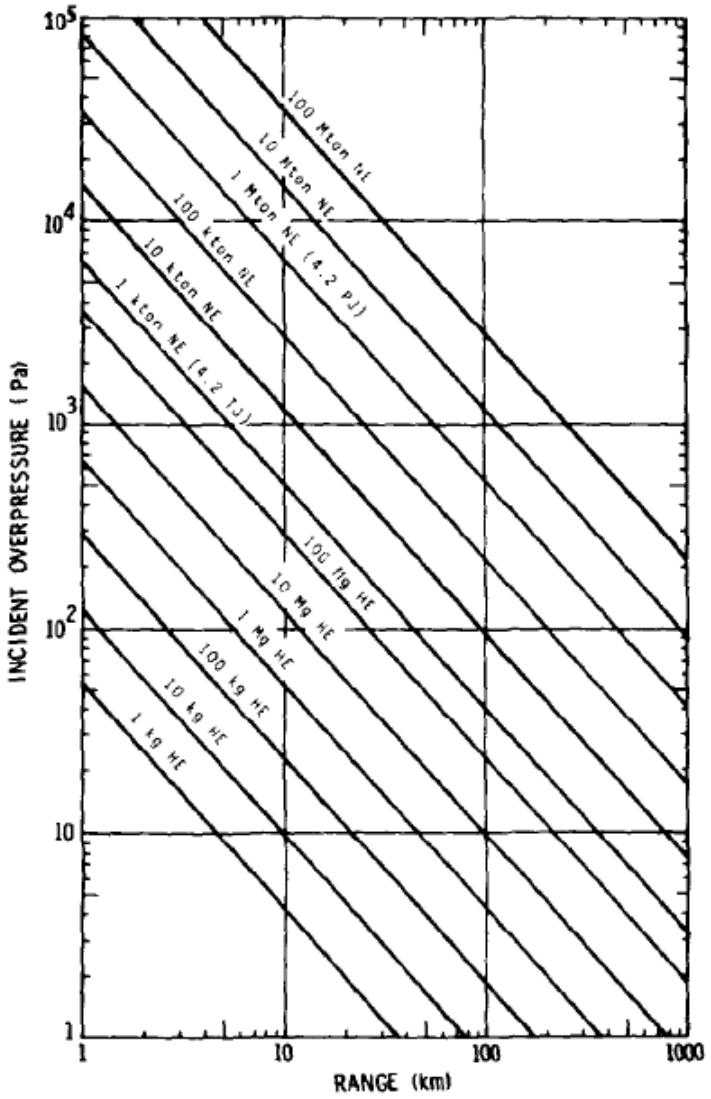

Figure 2-12: The figure shows the standard explosion curves for NE and HE yield taken from ANSI (2011).

Chapter 3

Shell Moerdijk explosions

The added value of measuring infrasound in 3D is found by analysing the Shell Moerdijk explosions. This chapter contains the observations of these Shell Moerdijk explosions. It describes the processing of infrasound data for two hours of data on 2014, June 03 starting at 20h01m34.861s Universal Time Coordinated (UTC) recorded at the KNMI infrasound array in Cabauw (CIA). This chapter first gives background information on the Shell Moerdijk explosions followed by the data description and the results of the array processing. Next, a detailed description of the signals in the Cabauw tower is given and the yield estimation.

3-1 Background

The facts of the Shell Moerdijk explosions are extracted from the report of the Onderzoeksraad (Onderzoeksraad, 2015). On 2014, June 03 at 22h48m26s Central European Summer Time (CEST) (i.e., at 20h48m26s UTC), a first explosion occurred at the MSPO-2 plant of Shell Moerdijk followed by a second explosion at 22h48m46s CEST. MSPO-2 plant stands for the second Monomer-Styrene-and-Propylene-Oxide plant. This plant produces basic chemicals like ethene and propylene, and these chemicals are used to create plastic products. A massive fire with lots of smoke took place after the explosions, which could be seen at large distances. Parts of the plant have been found at 250 meters distance, and the explosions could be heard 20 km away.

The explosions were caused by increased pressure in the catalyst during the heating process of the installation after maintenance. Maintenance is seen as a risky process as much can go wrong. The temperature and pressure increased incredibly in a very short time due to reactions between the ethyl-benzene and the catalyst in the reactor. The early warning signs were noticed too late, which made it impossible to drain the new build up gas and pressure. The situation became unruly causing the installation to explode. As this happened late in the evening, only two people were injured.

The MSPO-2 Shell Moerdijk plant has the coordinates N51° 40.873', E004° 34.168' in Geographic Coordinate System (GCS) (or in Rijksdriehoek (RD) x:98447 [m], y:410587 [m])

shown in figure 3-1. The tower in Cabauw has the coordinates N51° 58.216', E4° 55.572'. The true azimuth between the meteorological tower in Cabauw and the Shell Moerdijk plant is 217.5° located 40.5 km apart. The true azimuth between the receiver and the source is useful to know as it can give information on the propagation conditions of the atmosphere if compared with the back azimuth of the data.

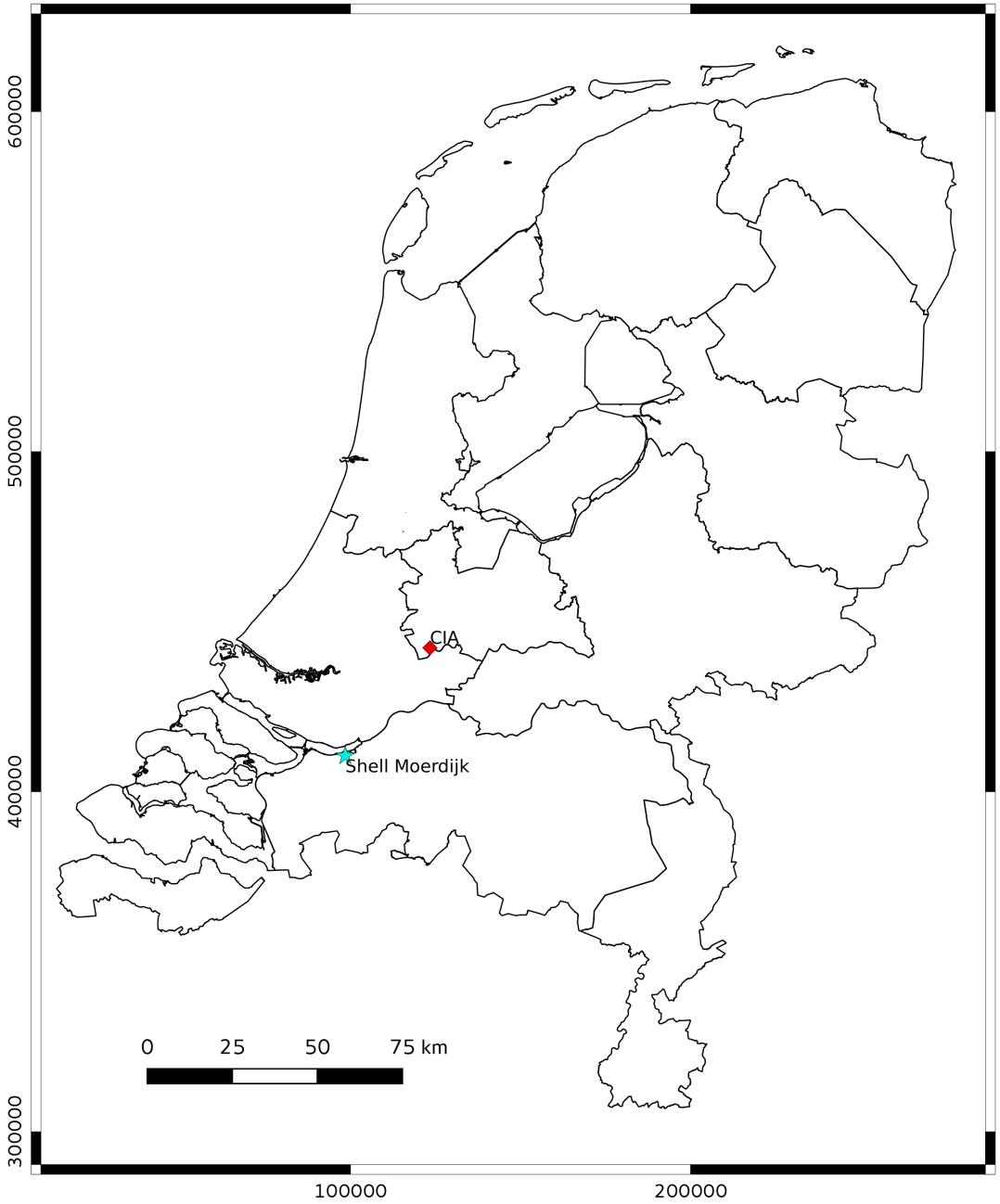

Figure 3-1: The map shows the location of the MSPO-2 Shell Moerdijk plant and the infrasound array CIA in the Netherlands in RD coordinate system.

3-2 Data description

The Cabauw Infrasound array is situated in the Netherlands. The CIA contains 15 elements of which ten are ground sensors, and five are tower sensors. The tower sensors reach a height up to 200 meters. The layout of the ground array is shown in figure 2-3 and it has an aperture of 700 meters. The ground sensors seven and nine were not working correctly during the time of the explosions. Therefore, these two sensors are not incorporated in further processing steps.

The raw infrasound recordings of all sensors of CIA are shown in figure 3-2 sampled at 40 Hz as described in Mentink & Evers (2011). The records of two hours of data start on 2014, June 03 at 20h01m34.861s UTC. During these two hours, two explosions at Shell Moerdijk took place. The raw recordings are bandpass filtered with a 2^{nd} order Butterworth filter having the corner frequencies 0.1 and 5 Hz. Figure 3-3 shows the filtered recordings for eight ground elements between 20h50m20s-20h51m00s UTC. The time axis is adjusted to demonstrate the signal's coherency, and the two arrivals between 20h50m20s-20h51m00s UTC contain the highest amplitude and coherency in the raw recordings. The filtered tower signals will be shown in section 3-4. The arrival time at CIA of the first signal is around 20h50m25s UTC and of the second signal is around 20h50m45s UTC. The time difference between the arrival time of the signal at CIA and the origin time of the explosion is 119 seconds. It will be investigated whether the Shell Moerdijk explosions caused these signals.

3-3 Data processing

The data is processed in the following way to identify the infrasound signals of the Shell Moerdijk explosions. The coordinates of the sensors are loaded to perform the Fisher analysis. The data is split into discrete windows (i.e., the bins). The binsize is determined by the aperture of the array and an apparent velocity of 142 m/s. This apparent velocity is resolved on the corners of the slowness grid for a p_x and p_y of 0.005 s/m. The binsize in the time domain can not be too small as the infrasound signal needs time to travel across the array. This ensures the correct resolvent of the time shifts. The binsize in the frequency domain can be made smaller as it performs a phase shift instead of a time shift. The bins are 50% overlapped. A slowness grid of 50×50 is utilised for the beamforming from -0.005 s/m to 0.005 s/m. Therefore, 2500 beams are evaluated for each bin/window.

The Fisher analysis is performed, and the F-ratio, apparent velocity and back azimuth are found for each time window. In 3D, the vertical incidence angle is determined additionally for each time window. The best beam is constructed based on the slowness vector corresponding to the maximum F-ratio. The scripts containing the 2D data processing steps are added in appendix A-2 and A-3 for respectively the time analysis and the frequency analysis. The 3D processing scripts are not added, as they are almost the same except for adding an extra dimension.

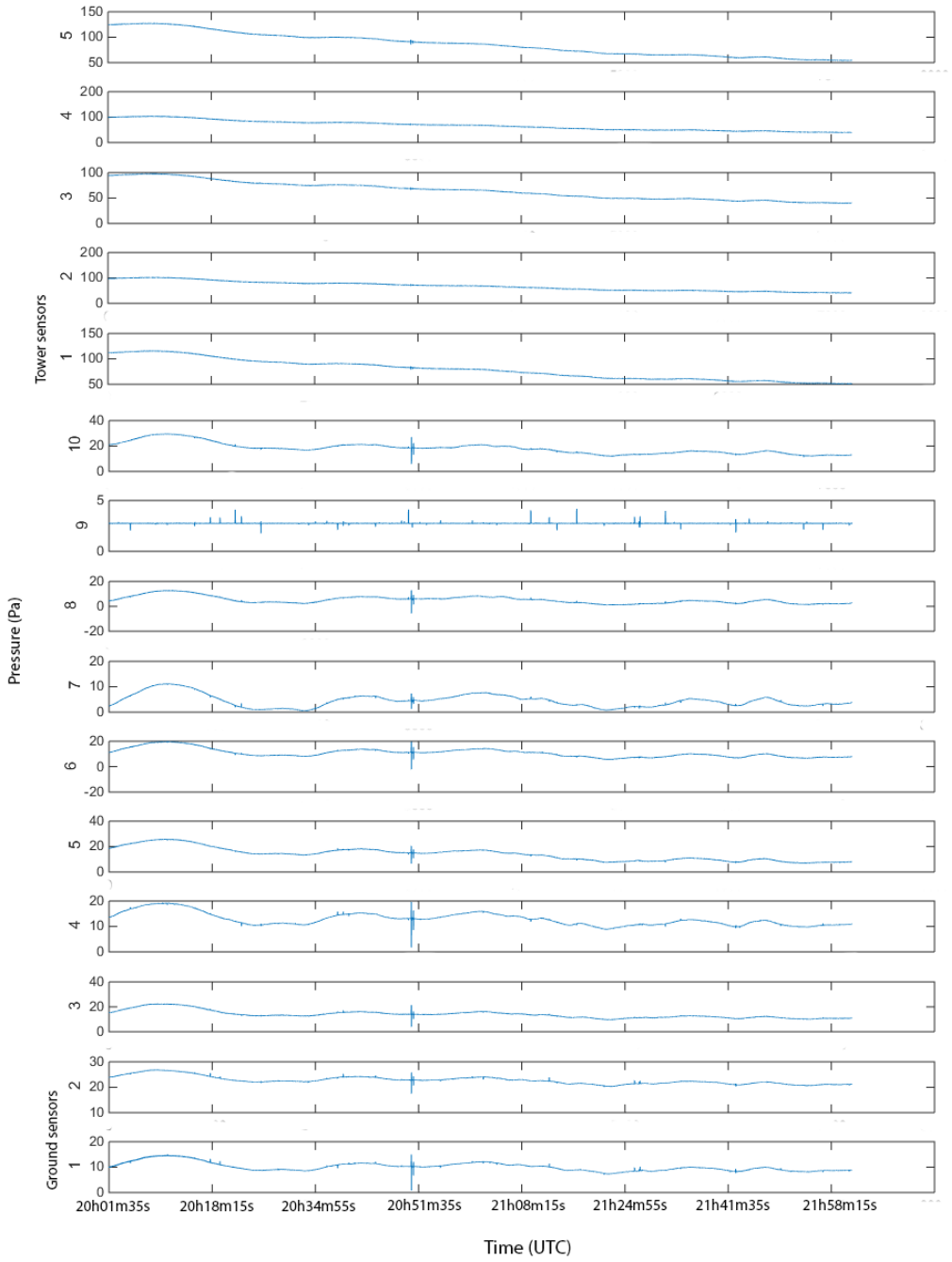

Figure 3-2: The unfiltered signals of the all sensors at CIA are shown. The time axis starts on 2014, June 03 at 20h01m34.861s UTC. The arrivals with the highest amplitude are in between 20h50m20s-20h51m00s UTC. The five top panels show the unfiltered signals of the tower sensors and the bottom ten panels are the unfiltered signals of the ground sensors.

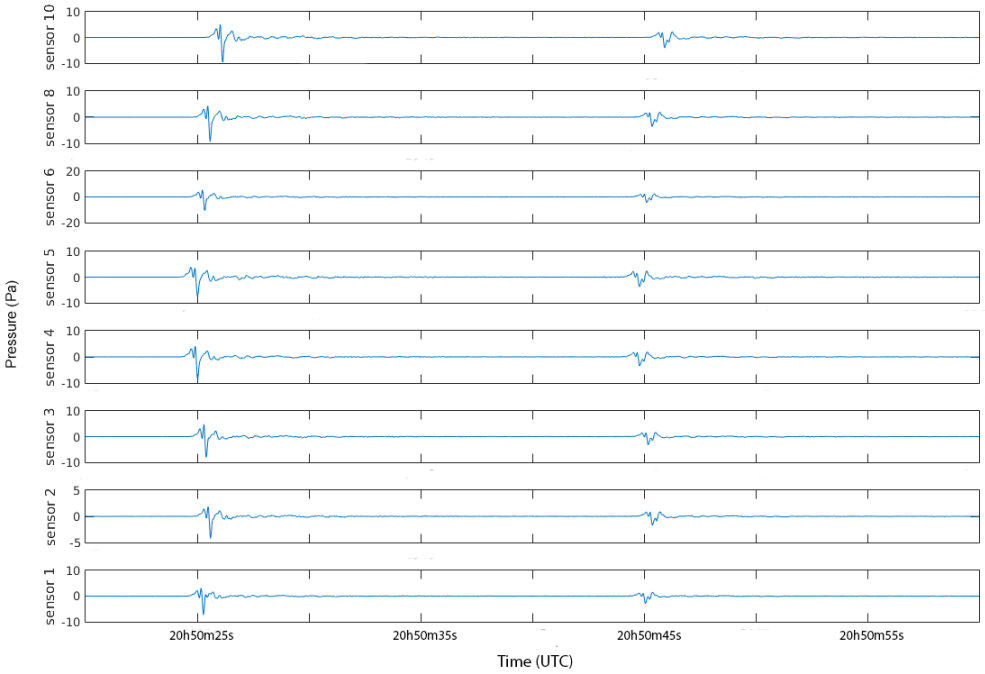

Figure 3-3: The filtered signals of the ground sensors at CIA are plotted. The signals are filtered with a 2^{nd} order Butterworth filter with the corner frequencies of 0.1 and 5 Hz.

3-3-1 Time domain analysis

The 2D time domain analysis uses the recordings of the ground sensors. The F-ratio as described in equation 2-16 is used to process the filtered recordings. The result of the 2D Fisher detection and processing is shown in figure 3-4. The 2D time Fisher analysis has a binsize of 200 samples, which is 5 seconds for a sample rate of 40 Hz.

A maximum F-ratio value of 67 is found at 20h50m25s UTC. By using equation 2-17, a snr^2 of 8.3 is calculated with the maximum F-ratio value. The second high F-ratio value is found after 20 seconds at 20h50m45s UTC. The F-ratio is 65 corresponding to a snr^2 of 8.0. The increase in F-ratio detects the infrasound of the explosions, as displayed in the lower frame of figure 3-4. The retrieved back azimuth and apparent velocity are 219.6° and 328.5 m/s for both the first and second arrival shown in the middle frames. A coda of infrasound after the explosions lasts for 130 s indicated with a stable back azimuth and apparent velocity. Two small increases in the F-ratio are visible at the end of the coda. The resolved back azimuth and apparent velocity correspond to a p_x and p_y of -0.0019 s/m and -0.0023 s/m respectively. The best beam is constructed with the slowness values at the maximum F-ratio. The normalised spectrogram took the highest amplitude as 0 dB reference value causing all spectral information being displayed as a negative dB amplitude. The characteristics of the 2D time Fisher analysis as used for CIA are listed in table 3-1.

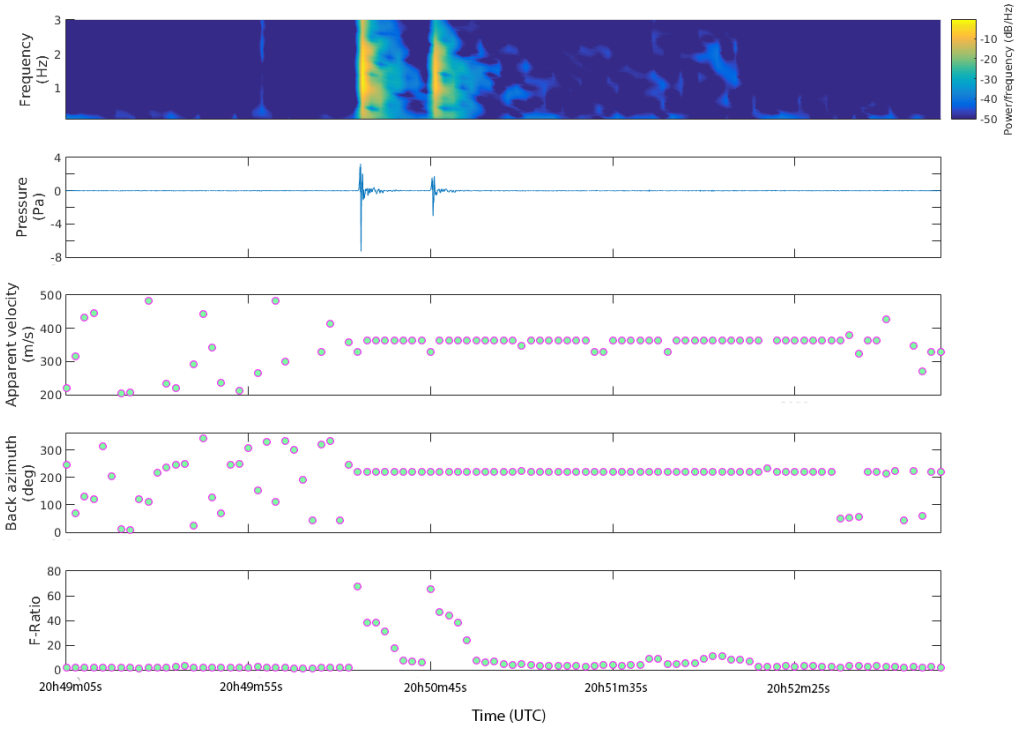

Figure 3-4: The result of the 2D time domain array processing. From top to bottom are shown the spectrogram, the best beam, the apparent velocity in m/s, the back azimuth in degrees and the F-ratio.

Table 3-1: 2D time Fisher analysis infrasonic observations and parameters

	CIA (1st / 2nd arrival)
Elements	8
Binsize	200
Bin overlap (%)	50
Sample rate (Hz)	40
Apparent veloity (m/s)	328.5
Back azimuth (deg)	219.6
Peak-to-peak amplitude (Pa)	10.5 / 4.7
p_x (s/m)	-0.0019
p_y (s/m)	-0.0023
Max. F-ratio	67 / 65
snr^2	8.3 / 8.0

The 3D time domain analysis uses the recordings of the ground and tower sensors. The results of the 3D time Fisher analysis are shown in figure 3-5. The same parameters, like binsize, overlap and slowness grid-size, are used in the 3D time analysis as in the 2D time analysis. From figure 3-2, it can be seen that the tower signals differ from the ground signals. The tower signals will be analysed in more detail in section 3-4. The number of working sensors is 13; these are eight ground sensors and five tower sensors.

The maximum F-ratio of 94 is found at 20h50m45s UTC related to a snr^2 of 7.2. The F-ratio is shown in the lower panel of figure 3-5. It resolves a back azimuth, an apparent velocity and a vertical incidence angle of 219.6°, 328.5 m/s and -45.4° respectively, plotted in the middle frames. These values correspond to p_x, p_y and p_z of -0.0019, -0.0023 and -0.0030. The peak-to-peak amplitude is 3.4 Pa. A second high F-ratio value of 53 is found at 20h50m25s UTC corresponding to a snr^2 of 4.0. The retrieved back azimuth, apparent velocity and vertical incidence are 219.6°, 328.5 m/s and -45.4° respectively. It relates to a p_x, p_y and p_z of -0.0019, -0.0023 and -0.0030. The best beam shows at 20h50m25s UTC a peak-to-peak amplitude of 6.5 Pa.

3-3-2 Frequency domain analysis

The 2D frequency domain analysis uses the recordings of the ground sensors. The F-ratio for the frequency domain as described in equation 2-18 is used. The results of the 2D frequency Fisher analysis are given in figure 3-6. The frequency band of interest is set from 0.1-3 Hz, in which the Fisher analysis is performed. The filtered data is split in 160 samples which correspond to a time window of 4 seconds for a sample rate of 40 Hz. A Hanning window is added to avoid Fast Fourier Transform (FFT) errors as spectral leakage. The frequency resolution is enhanced by zero-padding each window/bin. A padding factor (pf) of 1 is chosen. This means that for a bin of 160 samples, 320 zeros are added in the FFT. The number of zeros is calculated by binsize$\cdot 2^{pf}$.

The maximum F-ratio of 109 is found at 20h50m25s UTC corresponding to a snr^2 of 13.5. It resolves a back azimuth ϕ and apparent velocity c_{app} of 219.6° and 328.5 m/s respectively

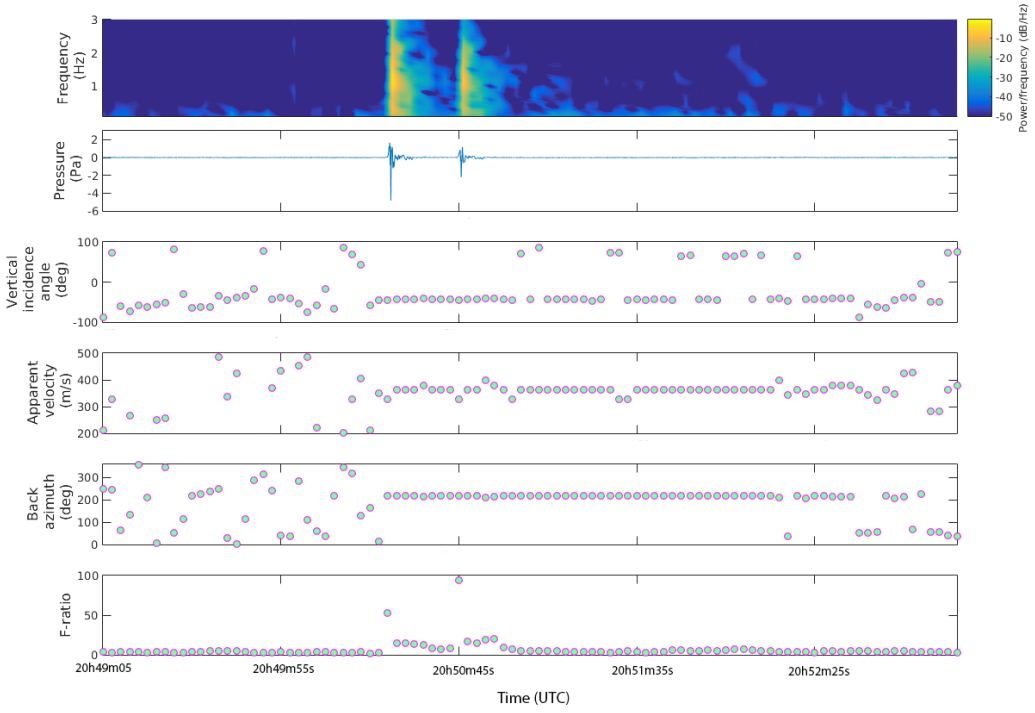

Figure 3-5: The result of the 3D time domain array processing. From top to bottom are shown the spectrogram, the best beam, the vertical incidence in degrees, the apparent velocity in m/s, the back azimuth in degrees and the F-ratio.

around 1 Hz. The second arrival has an F-ratio of 108 with a snr^2 of 13.4 at 20h50m45s UTC. The retrieved back azimuth and apparent velocity are the same as the first arrival around 1 Hz. These values follow from a p_x and p_y of -0.0019 and -0.0023 s/m. The best beam is constructed with these p_x and p_y. Table 3-2 gives the characteristics of the 2D frequency Fisher analysis as used for CIA.

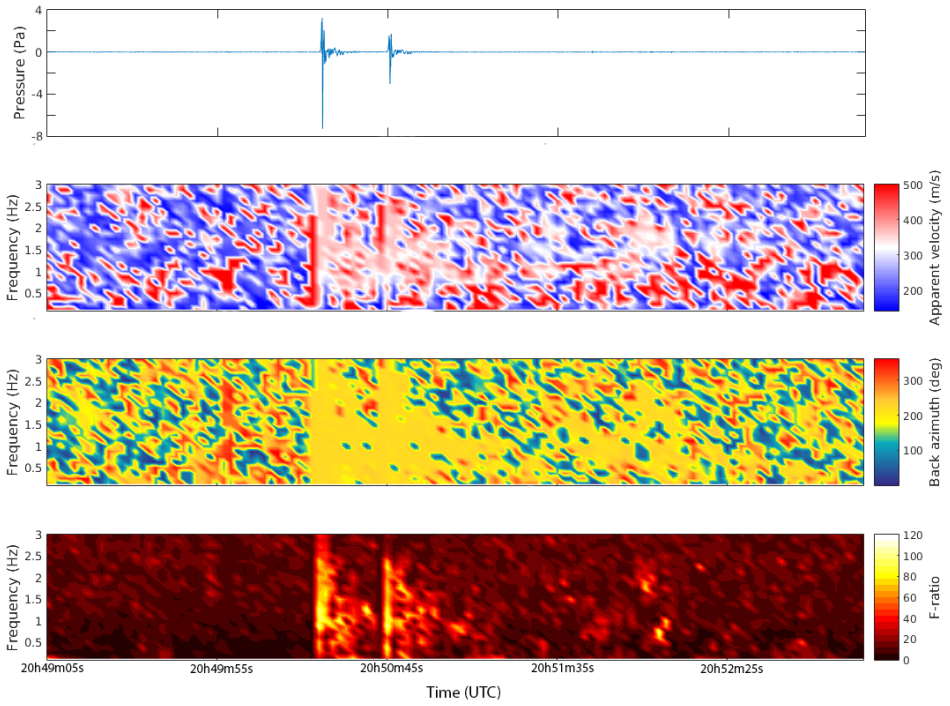

Figure 3-6: The result of the 2D frequency domain array processing. From top to bottom are shown the best beam, the apparent velocity in m/s, the back azimuth in degrees and the F-ratio.

The 3D frequency domain analysis uses the recordings of the ground and tower sensors. The results of the 3D frequency Fisher analysis is shown in figure 3-7. The same parameters are used in the 3D frequency analysis as the 2D frequency analysis. The working microbarometers are 13; these are eight ground sensors and five tower sensors.

The maximum F-ratio of 155 is located at 20h50m33s UTC for a p_x, p_y and p_z of -0.0007, -0.0015 and -0.0026 s/m respectively. However, at 20h50m33s UTC, neither of the two signals are found. Examining the F-ratio at the time of the signals, it gives an F-ratio of 77 at 20h50m25s UTC for a p_x, p_y and p_z of -0.0015, -0.0021 and -0.0034 s/m and a snr^2 of 5.8. It resolves a back azimuth, an apparent velocity and a vertical incidence angle of 215.5°, 379.7 m/s and -38.0° respectively. The best beam shows at 20h50m25s UTC a peak-to-peak amplitude of 3.1 Pa. At 20h50m45s UTC, the maximum F-ratio is 82 for a p_x, p_y and p_z of -0.0017, -0.0021 and -0.0036 s/m resolving a back azimuth, an apparent velocity and a vertical incidence angle of 219°, 362.7 m/s and -37.6° respectively. The snr^2 is 6.2 at 20h50m45s UTC and the peak-to-peak amplitude is 1.9 Pa in the best beam.

Table 3-2: 2D frequency Fisher analysis infrasonic observations and parameters

	CIA (1st / 2nd arrival)
Elements	8
Binsize	160
Overlap (%)	50
Sample rate (Hz)	40
Padding factor	1
Frequency band (Hz)	0.1-3
Apparent velocity (m/s)	328.5
Back azimuth (deg)	219.6
Frequency max. F-ratio (Hz)	1
Peak-to-peak amplitude (Pa)	10.5 / 4.7
p_x (s/m)	-0.0019
p_y (s/m)	-0.0023
Max. F-ratio	109 / 108
snr^2	13.5 / 13.4

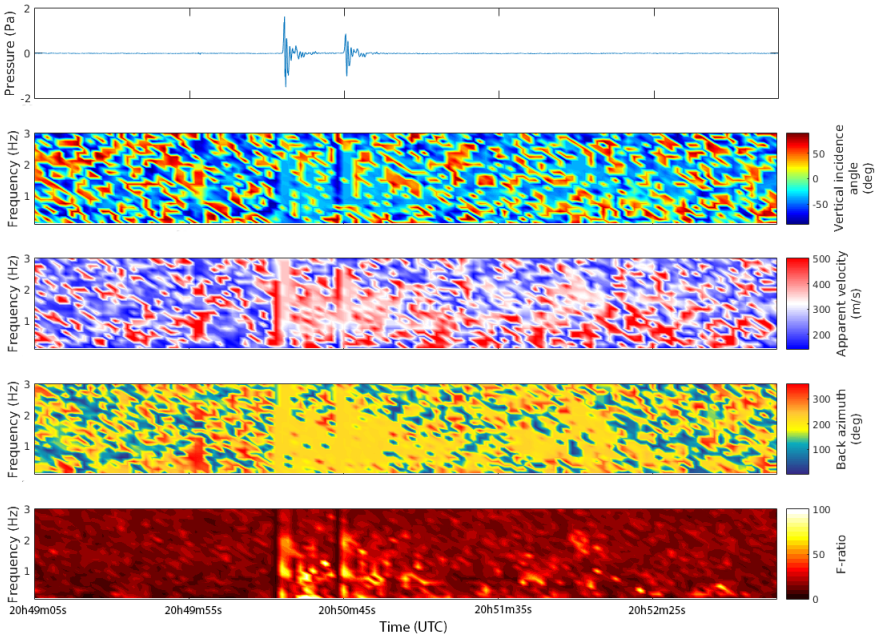

Figure 3-7: The result of the 3D frequency domain array processing. From top to bottom are shown the best beam, the vertical incidence in degrees, the apparent velocity in m/s, the back azimuth in degrees and the F-ratio.

3-4 Cabauw tower observations

The added value of measuring infrasound in 3D can be inspected by investigating the signature of the infrasound waveform with altitude in more detail. The filtered signals of Cabauw tower are plotted in figure 3-8. This figure also includes the best beam from the ground sensors in the lower panel. By comparing the towers signals with the best beam of the ground signals, it shows the signals differ significantly. The signals from the tower sensor are of a lower frequency than the ground signal. Three or two distinct peaks are visible per signal arrival in the tower data. This distinction is hard to see in the ground signals.

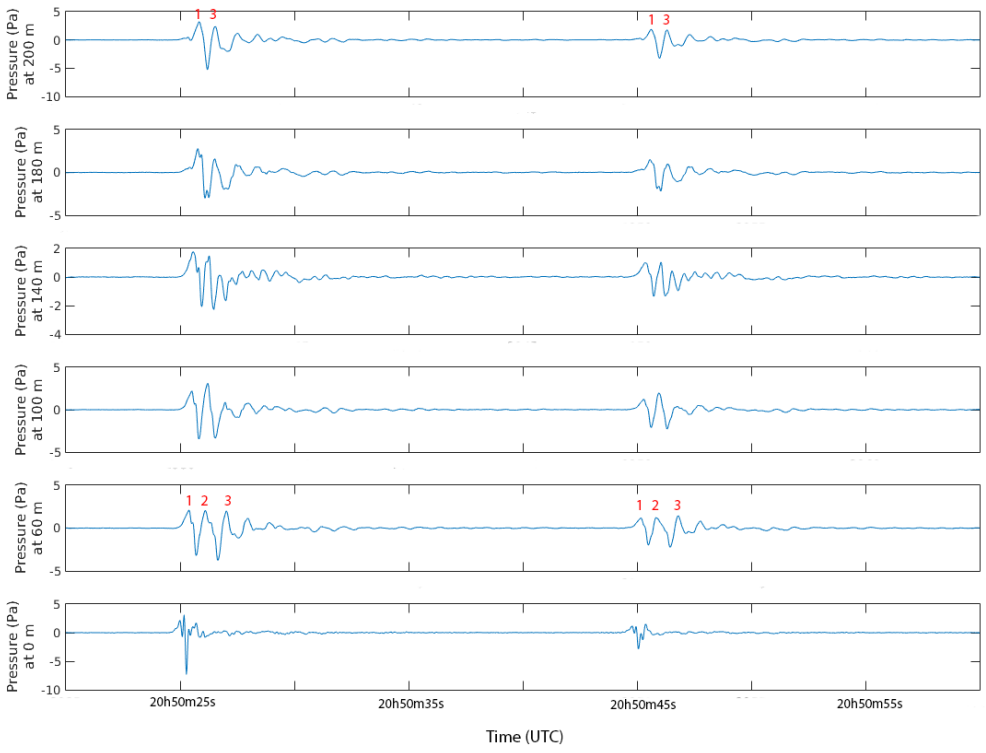

Figure 3-8: The top five panels contain the filtered signals of the Cabauw tower at different heights. The bottom panel consists the best beam of the ground sensors for comparison. The red numbers indicate the different peaks. The signals are filtered with a 2^{nd} order Butterworth filter with the corner frequencies of 0.1 and 5 Hz.

When examining the peaks of each signal in more detail, both signals seem to have three peaks at 60 meters height and two peaks at 200 meters height. For a better insight, the travel times differences for each peak for each signal with respect to the first arrival at the lowest level are taken and listed in table 3-3. The peaks are identified by their signature to make sure the same peaks are selected at the next altitude. Table 3-3 shows that peak one arrives first at 60 meters altitude and later at 200 meters altitude, while peak three appears first at 200 meters height and later at 60 meters height. Peak two appears first at 60 meters height and later at 140 meters altitude to disappear at higher altitudes.

Table 3-3: Travel time differences with respect to the first arrival at the lowest level

Travel time differences						
	Arrival one			**Arrival two**		
h (m)	peak 1 (s)	peak 2 (s)	peak 3 (s)	peak 1 (s)	peak 2 (s)	peak 3 (s)
60	0	0.700	1.625	19.800	20.450	21.380
100	0.125	0.825	1.575	19.900	20.575	21.350
140	0.175	0.875	1.275	19.975	20.650	21.125
180	0.375	-	1.125	20.175	-	20.925
200	0.450	-	1.125	20.225	-	20.900

By combining the travel times with height, the incidence angle can be determined for a range of altitudes. The incidence angles for the two major peaks are arranged in table 3-4 and shows that the incidence angle is changing for different altitude ranges. When combining the incidence angles with the travel times of the signals and adding the time of the Shell Moerdijk explosions, the path of the signals can be visualised. A rough estimate of the path of the signals is shown in figure 3-9. The y-axis is the altitude in meters and the x-axis the time in UTC. Ray tracing needs to be performed to confirm the possible explanation of the infrasound signals.

Table 3-4: The incidence angles obtained by travel times in Cabauw tower

Incidence angle (θ)				
	Signal 1		**Signal 2**	
h(m)	peak 1 (°)	peak 3 (°)	peak 1 (°)	peak 3 (°)
60-100	3.8	-1.9	3.7	-2.3
100-140	1.9	-9.9	2.4	-7.3
140-180	6.9	-5.3	6.5	-6.6
180-200	5.8	-1	3.0	-2.3
average	4.6	-4.5	3.9	-4.6

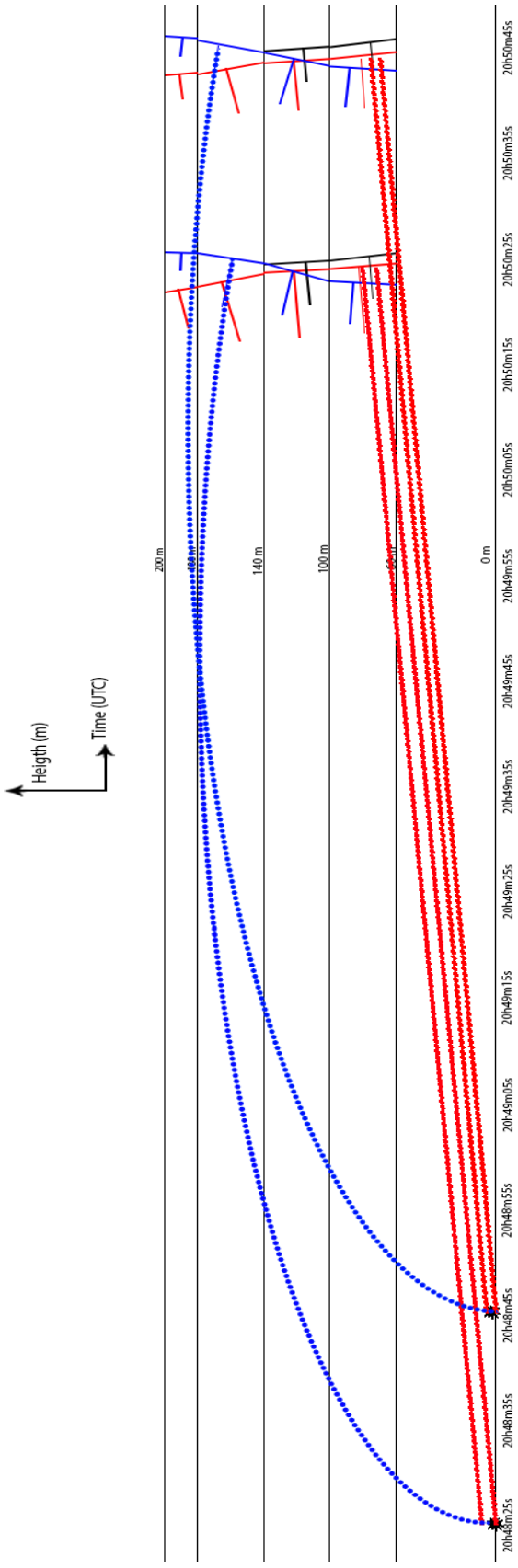

Figure 3-9: The figure shows a rough estimate of the infrasound travel path of the two major signals. The path is based on the travel time observations at the Cabauw tower in UTC, the time of the explosions in UTC and the incidence angle in degrees. The blue line indicates the travel path of the down-going waves and the red line the up-going waves.

3-5 Yield estimation

The yield of the explosion is determined by using equation 2-48 and the yield units in table 2-1. Figure 3-10 corresponds to the yield estimates. For the incident overpressure, an average value of maximum positive deviation from ambient pressure in the explosion wave of the ground signals is taken. The mean value is used for both the first and second arrival. The tower signals are excluded as the signals differ too much from the ground signals. The incident overpressure of the first explosion and the second explosion is 6.15 Pa and 2.78 Pa respectively.

When adding the peak blast overpressure of explosion one and two, measured at 40487 m from the source, in figure 3-10, it can be seen that explosion one has a strength of 185 kg HE, while explosion two has a yield of 21 kg HE.

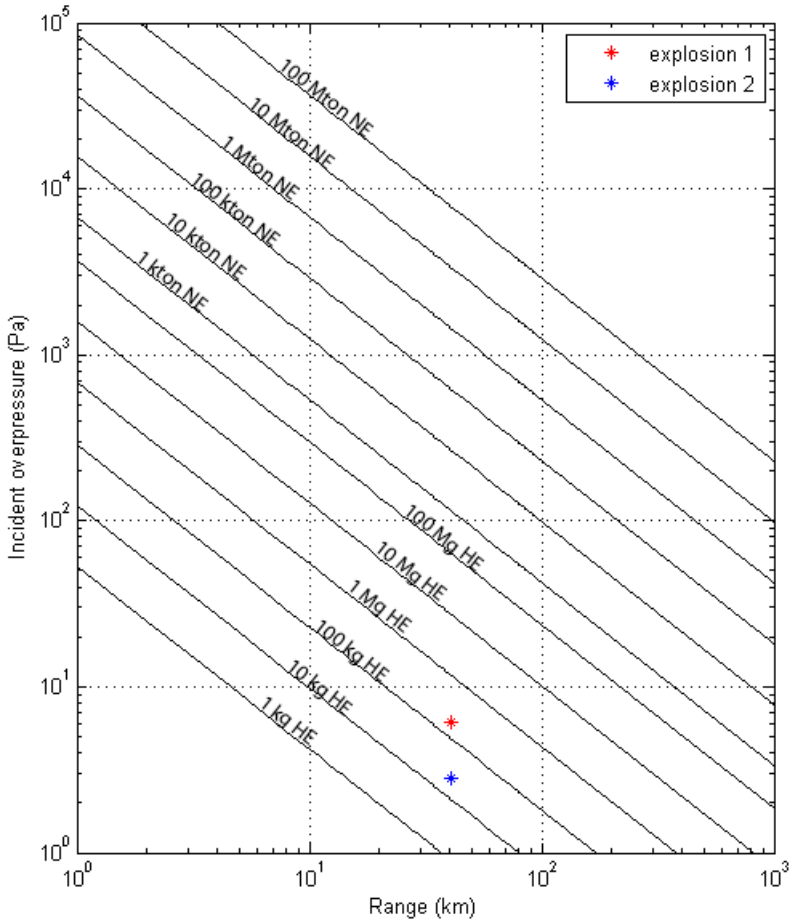

Figure 3-10: The result of the yield estimation of the two Shell Moerdijk explosions.

Chapter 4

Propagation modelling of the Shell Moerdijk detections

This chapter gives a possible explanation for the shallow refracted waves and the direct waves in chapter 3-4 caused by the Shell Moerdijk explosions. This explanation of the infrasound waves is found by propagation modelling (i.e., ray tracing). First, the different atmospheric datasets are compared followed by the results of the ray tracing.

4-1 Atmospheric datasets

For the ray tracing, an atmospheric dataset is needed. In the atmospheric dataset, information on the temperature and the wind with altitude is given, and this can be used to calculate the effective sound speed as in equation 2-28. The effective sound speed profile creates a layered atmosphere in which the infrasonic waves are refracted. Different atmospheric datasets are provided by the KNMI and European Centre for Medium-Range Weather Forecast (ECMWF) around the time of the explosions. Four different datasets are compared: two atmospheric models, one point measurement and one in-situ measurement. The datasets are:

1. The ECMWF High-Resolution Atmospheric Model (ECMWF HRES) global analysis is general circulation model. It has a horizontal resolution of ∼16 km with 137 vertical levels up to 1 Pa (∼80 km). It provides data every six hours. The ECMWF is based in Reading, UK (ECMWF, 2016).
2. The KNMI HARMONIE regional weather forecast model headquartered in the Netherlands has a horizontal resolution of ∼2.5 km with 60 vertical levels up to 100 Pa (∼40 km). The HARMONIE model is specially made for short-term weather forecast within major European cooperation projects. It produces data every hour (KNMI, 2016).
3. The 1290 MHz LAP3000 profiler based in Cabauw, the Netherlands, is a point measurement. It has a range in height for the temperature of 1.1 km and wind of 1.8 km.

The range resolution is 100 meters, and it depends on radar and atmospheric characteristics. It measures wind and temperature every 5 minutes but provides an average dataset of one hour. The profiler sends short radar pulses, and the signal returning from the atmosphere is processed (Cesar, 2016).

4. The Cesar Observatory based at the Cabauw site in the Netherlands is an in-situ measurement. It provides the true state of the atmosphere every 10 minutes at the coordinates 51.971° N, 4.927° E. It observes wind and temperature with time as a function of altitude up to 200 meters. The observed data from Cesar is used to check for variations in the atmospheric models (Cesar, 2016).

The two atmospheric models, the point measurement and the in-situ measurement are plotted in figure 4-1 up to 1200 meters altitude. In figure 4-1, the Cesar Observatory shows data at 20h50m UTC on 03-06-2014, the LAP3000 profiler contains an average data between 20h00m UTC and 21h00m UTC on 03-06-2014, the KNMI HARMONIE includes a dataset at 20h00m UTC on 03-06-2014, and two ECMWF HRES datasets are plotted at 18h00m UTC on 03-06-2014 and 00h00m on 04-06-2014. The point measurement of the LAP3000 profiler comes closest to the truth of the atmosphere measured by the Cesar Observatory, and it is, therefore, used for the ray tracing.

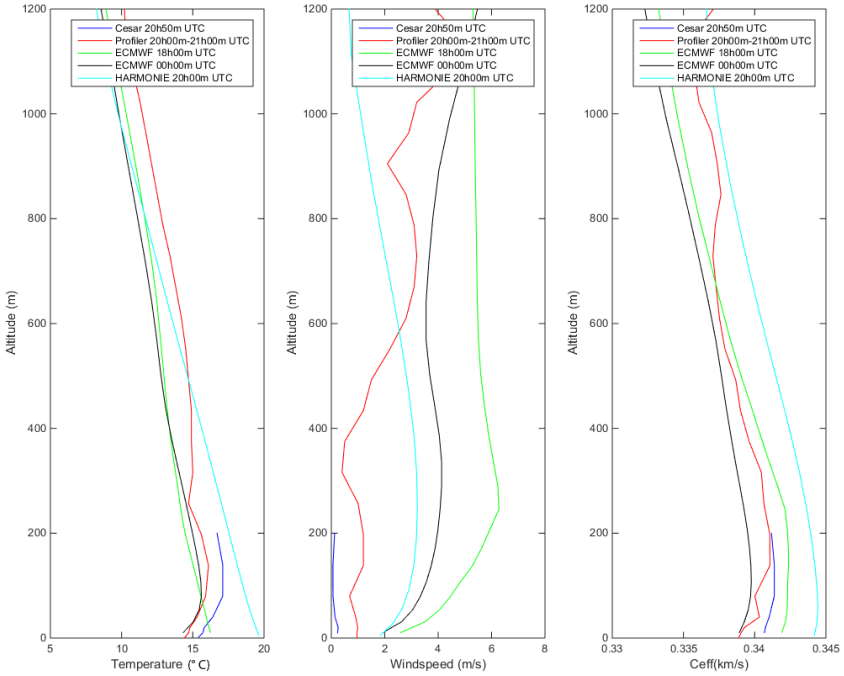

Figure 4-1: The two atmospheric models, the point measurement and the in-situ measurement are plotted. The Cesar Observatory in-situ measurement, the LAP3000 profiler point measurement and the KNMI HARMONIE model show the temperature and the wind around the time of the explosion, while the ECMWF HRES has data at 18h00m on 2014, June 03 and 00h00m UTC on 2014, June 04 exclusively.

The ECMWF HRES has an average data of six hours at 18h00m and 00h00m UTC exclusively, while the other datasets have data around the time of the explosion. The time resolution of the ECMWF HRES can be checked by comparing it with average data of six hours of the Cesar Observatory dataset. This comparison shows the quality of the ECMWF HRES with respect to the true atmosphere shown in figure 4-2. The Cesar Observatory point measurement is averaged between 15h00m UTC and 21h00m UTC on 2014, June 03. It can be seen that when taking an average of six hours of Cesar data, the temperature profile is similar to the ECMWF model at 18h00m UTC on 2014, June 03, but differs from the ECMWF model at 00h00m UTC on 2014, June 04. The wind profile of the Cesar Observatory seems to differ from both ECMWF models.

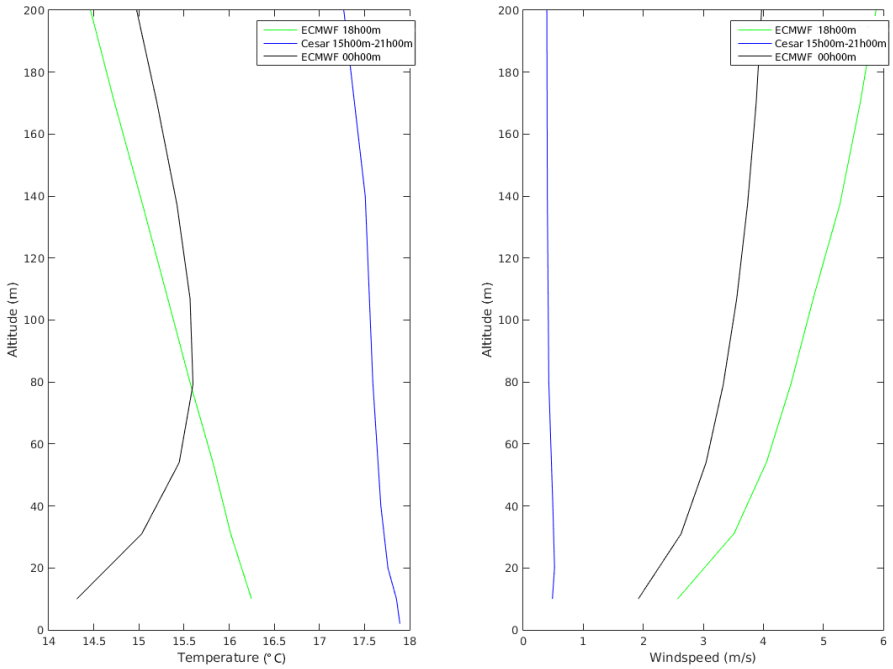

Figure 4-2: The Cesar Observatory point measurement averaged between 15h00m UTC and 21h00m UTC on 2014, June 03 is compared with the ECMWF models at 18h00m UTC on 2014, June 03 and at 00h00m UTC on 2014, June 04. The figure shows the temperature and the wind profile with altitude.

4-2 Propagation modelling results

The ray tracing is performed with the LAP3000 profiler dataset. The in-situ measurement of the temperature and the wind itself could not be used, as it has only data on five heights up to 200 m, while data from higher altitudes is needed. It also has no data for the ground conditions. Through the lack of data at the surface, numerical errors occurred during the ray tracing performance. The ray tracing results are presented in figure 4-3. The Matlab script of the ray tracing programmed the theory in chapter 2-2-3 and was provided by Ir. Pieter Smets

of the KNMI. A 1D atmosphere was assumed for the ray tracing in figure 4-3. The source is modelled at 0 km height with an azimuth of 37.5°. The launch angle is between 1° and 90° from the Earth's surface. The rays are plotted with an interval of 1° up to an altitude of 1.2 km. A range of 50 km is shown as the distance between the source and receiver is 40.5 km.

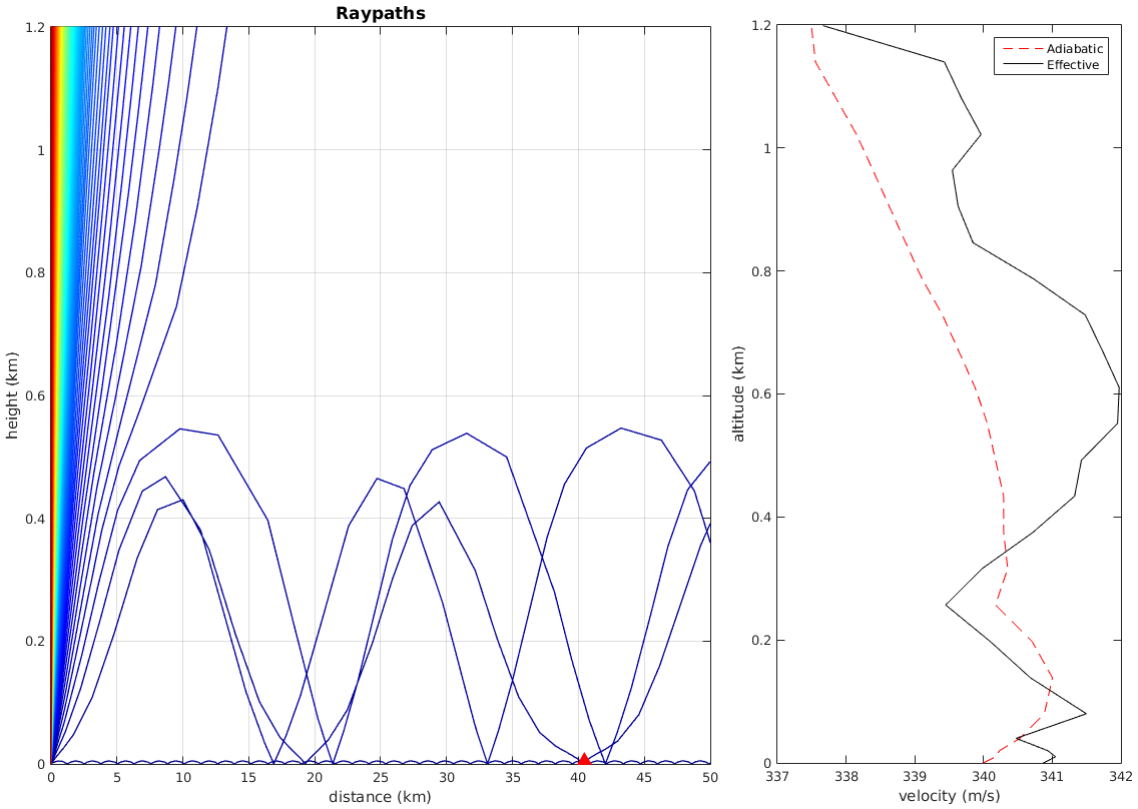

Figure 4-3: The ray tracing result with the LAP3000 profiler dataset containing average data of 20h00m and 21h00m UTC on 2014, June 03. The dark red indicates the rays with a launch angle around 90° from the Earth's surface. The colour shifts to dark blue symbolising the rays with a launch angle around 1° from the Earth's surface. The red triangle is the receiver position.

Figure 4-3 shows different ray paths through the atmosphere. A duct is formed around 500 meters height causing the infrasonic rays to bend to the Earth's surface and to reflect back into the air. These bends are caused by the increase of the wind with height. On the surface, a direct wave is visible travelling from the source to the receiver. At the source location, most rays are travelling vertically up into the atmosphere. The calculated travel time of the infrasound signals is 119 seconds based on an average effective velocity of 340 m/s and the source-receiver distance of 40487 m.

Chapter 5

Evaluation of the Shell Moerdijk explosions

This chapter contains the evaluation of the Shell Moerdijk explosions. Chapter 3 contains the results of the array processing, the investigation of the tower signals and the result of the yield estimation, while chapter 4 consists of the propagation modelling results. First, these obtained results are interpreted, followed by a summary of the case study.

5-1 Interpretation

The 2D time Fisher analysis, as well as the 2D frequency Fisher analysis, resolve for both signals a back azimuth of 219.6°. The true azimuth between the source and the receiver is 217.5°. The back azimuth has, therefore, a deviation of ±2.1° on the true azimuth. An explanation is the influence of tropospheric crosswinds on the infrasound signals, which deviated the rays to the West.

The next question is whether the two signals are two separated explosion signals or if the second signal came from the same explosion as the first signal but travelled a different path. From the 2D frequency Fisher analysis result, it was difficult to say which explanation is right. The result of the 2D time analysis shows that the apparent velocity of both signals is equal to 328.5 m/s. Therefore, the signals originate from two separated explosions. If the apparent velocity for both signals is different, the second signal has originated from the same explosion as the first signal. Moreover, the 2D Fisher analysis shows that the two distinct signals are separated by 20 seconds. This corresponds to the two explosions at Shell Moerdijk, which also occurred 20 seconds apart.

The estimation of the yield is for the first explosion 185 kg HE, and for the second explosion 21 kg HE. These values have to be seen as an order of magnitude. The estimate of the yield gives an explanation for why the first signal is stronger than the second signal; the explosion of the first signal is about nine times as powerful as the blast of the second signal.

In the result of the 2D time Fisher analysis, an extended coda after the first signal in the apparent velocity and back azimuth is visible. This coda is caused by the fire arising as a consequence of the explosions. This is observed as well in Evers et al. (2007) at a gas-pipeline explosion in Belgium. The two increases in F-ratio towards the end of the coda can come from small explosions at Shell Moerdijk during the fire.

During processing, a problem in the 2D frequency domain occurred with getting the right best beam for the data. The reason is that the 2D frequency Fisher domain is more sensitive to other signals than the time domain analysis, and these other signals also give a high Fisher value. The frequency domain analysis is narrowband, while the time domain is broadband, what prevents this problem. The problem was solved by forcing the frequency Fisher analysis to take the maximum F-ratio in a specific time window, where the signal is situated. This maximum Fisher value was then used to form the best beam.

A mistake was made in the frequency domain analysis. A binsize of 160 samples was taken to make the frequency step size as small as possible. But 160 is not a 2-to-the-nth-power number, which resulted in a long computational time for the FFT in the frequency analysis.

The frequency of the signals detected at the tower has been observed to be lower than the frequency of the signals detected at the surface. A possible reason is that the infrasound signal propagates through small pipes before reaching the tower sensors. As the frequencies of the tower signals are not in the same range anymore as the ground signals, the coherency between the signals is small. This causes the 3D Fisher analysis to be unsuccessful. Consequently, the back azimuth, the vertical incidence and apparent velocity were not able to resolve correctly. Although in the 3D time analysis, the back azimuth and apparent velocity were determined correctly, a vertical incidence angle of -45.4° is not logical. The vertical incidence angle can not be determined accurately due to the wrong estimation of p_z. Moreover, the 3D time Fisher analysis has a higher F-ratio for the second signal than for the first signal. It can be explained that the second signal has more coherency between the ground and tower signals than the first signal.

In the 3D frequency Fisher analysis, the first problem is that it resolves the maximum F-ratio at the wrong place. At the time of the signals, it solves a vertical incidence angle of -38°. The back azimuth and apparent velocity were not resolved correctly at both times in the frequency domain. Besides, the second signal has a higher F-ratio than the first signal again. The right p_x and p_y were applied, and even then, an incorrect vertical incidence angle was resolved. The results of the 3D analysis both in time and frequency, showed, due to lack of coherency, that the parameters can not be determined correctly.

Next, the Cabauw tower signals were investigated in more detail as they offer a better insight into the signature of the propagating waves. It showed two waves for the first signal: one wave is propagating upwards and one wave downwards originating from the same explosions. The same can be seen for the second signal. By analysing the angles obtained from the travel time differences, the upward propagating wave is a direct wave travelling through the atmosphere from source to the receiver. The downward propagating wave seems to be refracted from a shallow height in the atmosphere. The angels are changing at a certain range of altitudes caused by temperature and wind influences.

Noticeable is the negative p_z in the 3D time and frequency Fisher analysis; it represents the down-going wave. The up-going wave would have a positive p_z value. The up-going wave is not represented in the 3D Fisher analysis, although it is present in the tower signals.

Ray tracing confirms the possible infrasound signals in the Cabauw tower observations. The down-going wave comes from a refraction at 500 meters height. The up-going wave is the direct wave but bent slightly upwards by the wind and temperature. The up-going wave can also be a reflection of the infrasound wave at the surface, but the incidence angles from the tower signals are not confirming this hypothesis. The ray tracing solves a travel time of 119 seconds between the source and the receiver. The time difference between the origin time of the explosions (i.e., 20h48m26s and 20h48m46s UTC) and the recorded time at the CIA (i.e., 20h50m25s and 20h50m45s UTC) is also 119 seconds. As the travel times are the same, it shows that one duct was formed, and not two.

5-2 Summary of the case study

In summary, two infrasound signals were recorded at 20h50m25s and 20h50m45s UTC at the CIA. The 2D Fisher analysis showed that the two signals originated from two distinct explosions. The back azimuth of the 2D Fisher analysis confirms the source location to be Shell Moerdijk. The back azimuth has an azimuthal deviation of 2.1° caused by the influence of tropospheric crosswinds. The signals were recorded 119 seconds after the origin time of the explosions. The yield estimation illustrated that the first explosion was nine times stronger than the second explosion. The 3D Fisher analysis could not resolve the parameters correctly due to the lack of coherency between the ground and tower signals. Finally, the detailed examination of the tower signals revealed up- and down-going waves. The up-going wave is a direct wave, and the down-going wave is a refracted wave. Ray tracing confirmed the existence of these different waves.

Chapter 6

Discussion and conclusion

The infrasound signals from the Shell Moerdijk explosions have clearly been detected by the Cabauw Infrasound Array (CIA) in the Netherlands on 2014, 03 June. The Shell Moerdijk explosions are used as a case study and the results of this case study revealed the gained information on the 3D infrasonic wavefield. When comparing the recorded infrasound at the surface with the recorded infrasound in the tower, it shows that the tower signals are of a lower frequency than the ground signals. A possible reason is that the infrasound signal propagates through small pipes before reaching the tower sensors. As the ground and tower signals are no longer in the same frequency range, the coherency between the signals is poor. Due to this lack of coherency, the 3D Fisher analysis could not be performed correctly. However, the vertical tower measurements give valuable new information as it revealed up- and down-going waves for both explosions. The incidence angles unveil a slight refracted down-going wave and a direct up-going wave from the blasts. This is confirmed by the ray tracing result showing a duct at 500 meters, which causes the waves to refract back to the surface, and a direct wave along the surface.

In conclusion, to answer the research question whether measuring infrasound in 3D has an added value, it can be stated that measuring infrasound in 3D contributes to the full understanding of the 3D infrasonic wavefield. The tower signals showed up- and down-going waves for both explosion signals, which can only be seen in the 3D vertical measurements. The up-going wave is a direct wave from the source to the receiver, and the down-going wave is a refracted wave from 500 meters altitude.

Possible recommendations for further research are:

- Perform research to find a solution for the changing frequency of the tower signals. A possibility is to adjust the wind filters of the tower microbarometers. This can result in the tower signals remaining in the same frequency range as the ground signals.
- Perform ray tracing in higher dimensions as 2D or 3D, or perform full waveform modelling. This can give a more accurate result of the ray tracing. Ray tracing has been carried out in this research in 1D.

- Perform ray tracing with probabilistic atmospheric models instead of deterministic atmospheric models and investigate the results. It can give a different result. In this research, deterministic models were used.
- Investigate more recordings of infrasound signals in 3D and analyse the up-going and down-going waves in the infrasound to obtain a better knowledge on the 3D infrasonic wavefield. By measuring more infrasound signals in 3D, it will give insight whether it always has an added value or only in some cases.
- The Cabauw tower can be located in a zone of silence of the infrasound signal. Perhaps in the future, place more microbarometers in a tower at different locations to be able to measure every infrasound signal in 3D.

Bibliography

ANSI (2011). Estimating Airblast Characteristics for Single Point Explosion in Air, with a Guide to Evaluation of Atmospheric Propagation and Effects. *Technical Report ANSI, S2.20-1983*.

Assink, J., Averbuch, G., Smets, P., & Evers, L. (2016). On the infrasound detected from the 2013 and 2016 DPRK's underground nuclear tests. *Geophysical Research Letters*, *43*(7), 3526–3533.

Assink, J., Evers, L., Holleman, I., & Paulssen, H. (2008). Characterization of infrasound from lightning. *Geophysical Research Letters*, *35*(15).

Bedard, A. & Georges, T. (2000). Atmospheric infrasound. *ACOUSTICS AUSTRALIA*, *28*(2), 47–52.

Campus, P. (2004). The IMS infrasound network and its potential for detection of events: examples of a variety of signals recorded around the world. *Inframatics*, *6*, 14–22.

Campus, P. & Christie, D. (2010). Worldwide observations of infrasonic waves. In *Infrasound Monitoring for Atmospheric Studies* (pp. 185–234). Springer.

Ceranna, L., Le Pichon, A., Green, D., & Mialle, P. (2009). The Buncefield explosion: a benchmark for infrasound analysis across Central Europe. *Geophysical Journal International*, *177*(2), 491–508.

Cesar (2016). Instruments - active. http://www.cesar-observatory.nl/index.php?pageID=2000.

Davison, C. (1917). Sound-Areas of Great Explosions. *Nature*, *98*, 438–439.

Donn, W. L. & Ewing, M. (1962). Atmospheric waves from nuclear explosions. *Journal of Geophysical Research*, *67*(5), 1855–1866.

ECMWF (2016). Datasets. http://www.ecmwf.int/en/forecasts/datasets.

Edwards, W. N. & Green, D. N. (2012). Effect of interarray elevation differences on infrasound beamforming. *Geophysical Journal International*, *190*(1), 335–346.

Evers, L., de Bree, H., Haak, H., & Koers, A. (2000). The Deelen infrasound array for recording sonic booms and events of CTBT interest. *Journal of Low Frequency Noise, Vibration and Active Control*, *19*(3), 123–133.

Evers, L. G. (2008). *The inaudible symphony: on the detection and source identification of atmospheric infrasound*. PhD thesis, TU Delft, Delft University of Technology.

Evers, L. G., Ceranna, L., Haak, H. W., Le Pichon, A., & Whitaker, R. W. (2007). A seismoacoustic analysis of the gas-pipeline explosion near Ghislenghien in Belgium. *Bulletin of the Seismological Society of America*, *97*(2), 417–425.

Evers, L. G. & Haak, H. W. (2010). The characteristics of infrasound, its propagation and some early history. In *Infrasound Monitoring for Atmospheric Studies* (pp. 3–27). Springer.

Fee, D., Waxler, R., Assink, J., et al. (2013). Overview of the 2009 and 2011 Sayarim infrasound calibration experiments. *Journal of Geophysical Research: Atmospheres*, *118*(12), 6122–6143.

Garcés, M. A., Hansen, R. A., & Lindquist, K. G. (1998). Traveltimes for infrasonic waves propagating in a stratified atmosphere. *Geophysical Journal International*, *135*(1), 255–263.

Gibbons, S. J. & Ringdal, F. (2010). Detection and analysis of near-surface explosions on the Kola Peninsula. *Pure and Applied Geophysics*, *167*(4-5), 413–436.

Gitterman, Y. & Hofstetter, R. (2014). GT0 explosion sources for IMS infrasound calibration: charge design and yield estimation from near-source observations. *Pure and Applied Geophysics*, *171*(3-5), 599–619.

Green, D. N., Vergoz, J., Gibson, R., Le Pichon, A., & Ceranna, L. (2011). Infrasound radiated by the Gerdec and Chelopechene explosions: propagation along unexpected paths. *Geophysical Journal International*, *185*(2), 890–910.

Jensen, F. B., Kuperman, W. A., Porter, M. B., & Schmidt, H. (2011). *Computational ocean acoustics*. Springer Science & Business Media.

KNMI (2016). KNMI Norh Sea Wind atlas. https://www.knmi.nl/kennis-en-datacentrum/project/knmi-north-sea-wind-atlas.

Lin, F.-C., Ritzwoller, M. H., & Snieder, R. (2009). Eikonal tomography: surface wave tomography by phase front tracking across a regional broad-band seismic array. *Geophysical Journal International*, *177*(3), 1091–1110.

Marcillo, O., Arrowsmith, S., Whitaker, R., Morton, E., & Phillips, W. S. (2014). Extracting changes in air temperature using acoustic coda phase delays. *Journal of the Acoustical Society of America*, *136*(4), EL309–EL314.

Melton, B. S. & Bailey, L. F. (1957). Multiple signal correlators. *Geophysics*, *22*(3), 565–588.

Mentink, J. H. & Evers, L. G. (2011). Frequency response and design parameters for differential microbarometers. *The Journal of the Acoustical Society of America*, *130*(1), 33–41.

Nature (1922). Propagation of the Sound of Explosions. *Nature*, *110*, 619–620.

NOAA, N. (1976). USAF. US Standard Atmosphere, 1976. *US Government Printing Office, Washington, DC, USA*.

Olson, J. V. (2004). Infrasound signal detection using the Fisher F-statistic. *Inframatics*, *6*, 1–7.

Onderzoeksraad (2015). Explosies MSPO2 Shell Moerdijk. http://www.onderzoeksraad.nl/nl/onderzoek/2039/explosies-mspo2-shell-moerdijk/publicatie/1644/shell-moerdijk-moet-kritischer-zijn-op-veiligheid.

Rost, S. & Thomas, C. (2002). Array seismology: Methods and applications. *Reviews of geophysics*, *40*(3).

Smart, E. & Flinn, E. A. (1971). Fast frequency-wavenumber analysis and Fisher signal detection in real-time infrasonic array data processing. *Geophysical Journal International*, *26*(1-4), 279–284.

Ulivieri, G., Marchetti, E., Ripepe, M., Chiambretti, I., De Rosa, G., & Segor, V. (2011). Monitoring snow avalanches in Northwestern Italian Alps using an infrasound array. *Cold Regions Science and Technology*, *69*(2), 177–183.

Wexler, H. & Hass, W. (1962). Global atmospheric pressure effects of the October 30, 1961, explosion. *Journal of Geophysical Research*, *67*(10), 3875–3887.

Appendix A

Infrasound processing scripts

A-1 Array response

```
% Array response beamforming

%% read in data
clear all;
close all;
clc;

folder = '/run/media/woude/from_mos001_2tb/Thesis_3D_data/';

numbgs=10;  %number of ground sensors

%% Beamforming array response
    % read in coordinates
    A=load('/run/media/woude/from_mos001_2tb/Thesis_3D_data/coordinaten.txt');
    rx=A(1:numbgs,2)-mean(A(1:numbgs,2));
    ry=A(1:numbgs,3)-mean(A(1:numbgs,3));

    % define grid size
    gridx=50;
    gridy=50;

   %% define frequency
    f=0.4;
    w=2*pi*f;

    %define p0 if wanted to be added in script
%     phi_r=37.5;
%     Capp_r=350;
%     Pslow=1/Capp_r;
%
%     px0=Pslow*cosd(phi_r);
%     py0=Pslow*sind(phi_r);
%
    px0=0;
    py0=0;

    % instruments
    ninstr=length(rx);

    % array response
  for ii= 1:gridx;
      px = (-0.005+(0.01/(gridx-1))*(ii-1));
              for jj = 1:gridy;
                  py = (-0.005+(0.01/(gridy-1))*(jj-1));
                        for instr = 1:numbgs;
                                dtr= w.*((px-px0)*rx(instr)+(py-py0)*ry(instr));
                                ep(ii,jj,instr) = cos(dtr)-1i*sin(dtr);
                      end
              end
  end

% 2D
```

```
R=(abs((1/ninstr)*sum(ep(:,:,:),3))).^2;
Rnorm=R/max(max(R));

% 2D                                                                    56
    Px=linspace(-0.005,0.005,gridx);
    Py=linspace(-0.005,0.005,gridy);


%% Plot array response                                                  61


    figure;
    pcolor(Px,Py,Rnorm)
    title('Array Response');                                            66
    xlabel('px(s/m)')
    ylabel('py (s/m)')
    shading interp
    colorbar
                                                                        71
    figure;
    plot(rx,ry,'^','MarkerFaceColor',[.49 1 .63],'MarkerSize',10)
    title('coordinates measurements');
    ylabel('ry [m]');
    xlabel('rx [m]');                                                   76
```

A-2 2D Time domain Fisher Analysis

```
% Time Fisher Analysis
                                                                        2
clear;
close all;
clc;
tic
                                                                        7
%% read data
folder = '/run/media/woude/from_mos001_2tb/Thesis_3D_data/data/';
files = dir(fullfile(folder,'*.sac'));

numbg=8; %number of ground sensors                                      12

        for il=1:numbg
            x(il)=rdsac(files(il).name);
            raw(il,:)=x(il).d;
            time(il,:)=x(il).t;                                         17
            hdr(il,:)=x(il).HEADER;
        end

%% get headers parameters and visualize raw data
L = length(raw); % length of signal                                     22
fs= 40; % sampling frequency
ts = 1/fs; % sampling time
t = (0:ts:(L-1)*ts)';%calculate time axis
ninstr=size(raw,1); %number of instruments
                                                                        27
        figure;
        for ii=1:ninstr;
        subplot(ninstr,1,ii)
        plot(t,raw(ii,:))
        xlim([2929 2935])       % compare with filter data if correct filter is used    32
        end


%% filter data
% butterworth frequencies                                               37
[b1,a1] = butter(1,[0.1/(fs/2) 5/(fs/2)],'bandpass');

% filter data and substracting mean (detrend)
figure;
[dat,X,samples]=deal(zeros(ninstr,L));                                  42
for ii=1:ninstr;
    dat(ii,:)=raw(ii,:)-mean(raw(ii,:),2);      % detrending
    X (ii,:)= filter(b1,a1,dat(ii,:));
    samples(ii,:)=X(ii,:)-mean(X(ii,:),2);      % detrending after filter
    subplot(ninstr,1,ii)                                                47
    plot(t,samples(ii,:))                       % visualize filter data for check
    xlim([2925 2965])
end

samples=samples';                                                       52
%% load in coordinates
    A=load('/run/media/woude/from_mos001_2tb/Thesis_3D_data/coordinaten2.txt');
    rx=A(1:ninstr,2)-mean(A(1:ninstr,2));
    ry=A(1:ninstr,3)-mean(A(1:ninstr,3));
                                                                        57
    figure; %visualise coordinates
    plot(rx,ry,'o')
```

```
    title('coordinates measurements');
    ylabel('ry [m]');
    xlabel('rx [m]');

% define grid size
    gridx=50;
    gridy=50;

%% Set parameters for Fisher time Analysis
binsize=200;
n=100/50;   %100%/50% overlap, choose your overlap
nbins=floor(length(samples)/(binsize/n)); %number of bins
overlap=binsize/n;  %overlapping bins


T=binsize;
N=ninstr;
runs=nbins-2;
Px=linspace(-0.005,0.005,50);
Py=linspace(-0.005,0.005,50);
Constant=(T*(N-1))/(N*(T-1));

%% Run Fisher time analysis
[tt,Fratio,Capp,phi]=deal(zeros(nbins,1));
[Ftest]=deal(zeros(nbins,gridx,gridy));
[I2,I3]=deal(zeros(1,runs));
[Fmatrix,Fma_trans]=deal(zeros(binsize,ninstr));

for bin=2:nbins-2;
        ss=(bin-1)*overlap;
        es=ss+binsize-1;
        tt(bin)=(ss+es)/2*ts;
     for ii=1:gridx;
            px =(-0.005+(0.01/(gridx-1))*(ii-1));
              for jj =1:gridy;
                  py =(-0.005+(0.01/(gridy-1))*(jj-1));

                    for instr = 1:ninstr;
                                dt =-(px*rx(instr)+py*ry(instr));
                                ds=round((dt/ts));
                                ssi=ss+ds;
                                esi=ssi+(binsize-1);

                                %make time shifted matrix
                                Fmatrix(:,instr)=samples(ssi:esi,instr);
                    end

                    Fma_trans=Fmatrix';
                    F1= sum(sum(Fma_trans,1).^2,2);
                    F2=sum(sum(Fma_trans,1),2).^2;
                    F3=sum(sum(Fma_trans.^2,1),2);

                    Ftest(bin,ii,jj)=Constant*((F1-((1/T)*F2))/(F3-((1/N)*F1)));
              end
     end

    % max Fratio
        [Fratio(bin),I]=max(Ftest(bin,:));
        [I2(bin),I3(bin)]=ind2sub([gridx,gridy],I);
    % apparent velocity
          Capp(bin)=1/sqrt(Px(I2(bin))^2 + Py(I3(bin))^2);
    % back azimuth
            phi(bin)=atan2d(Px(I2(bin)),Py(I3(bin)));
            if phi(bin)<0
                phi(bin)=phi(bin)+360;
            else
                phi(bin)=phi(bin);
            end
end

%% windowing
w=hann(binsize);

%% Construct best beam
Matrix_Fpxpy=zeros(bin,3);
Matrix_Fpxpy(:,1)=Fratio(1:bin);
Matrix_Fpxpy(:,2)=I2';
Matrix_Fpxpy(:,3)=I3';


% Take the max F ratio value as it shifts the signals the best
[Fmax, position]=max(Matrix_Fpxpy(:,1));
BB_val=Matrix_Fpxpy(position,:);

Pxbeam=Px(BB_val(2));
Pybeam=Px(BB_val(3));
dtBB=-(Pxbeam.*rx+Pybeam.*ry);
dsBB= round((dtBB./ts));
start=binsize/n;    %starting place as time shift is the same
ssBB=start+dsBB;    %shifted samples with one Px and Py for all samples
```

```
esBB=es+dsBB;     %end shifted samples for all
lBB=(esBB(1)-ssBB(1))+1;  % length of BBtest

[BBtest]=deal(zeros(lBB,ninstr));
for instr =1:ninstr
BBtest(:,instr)=samples(ssBB(instr):esBB(instr),instr);
end

BestBeam=mean(BBtest,2);


%% frequency definition for spectrogram
%padding factor
pf=1;
Np=binsize*2^pf;

Nyquist=fs/2;

freq=(0:(Np/2)-1)*Nyquist/(Np/2);
wn=-2*pi.*freq;
freqmin=0.1;
freqmax=3;
[~,ifmin]=min(abs(freq-freqmin));
[~,ifmax]=min(abs(freq-freqmax));
fspec=freq(ifmin:ifmax);

%% Plot figures
xl1=2850;   %adjust time window to see signals clearly
xl2=3090;

% spectrogram needs different time window
ast=start*ts;
aet=es*ts;
tend=length(samples)*ts;
dif_s=(tend-aet)+ast;

%set correct time axis
tbegin=n*binsize/2*ts;
ttt=linspace(tbegin,tend,bin+1);

figure;
subplot(5,1,5)
plot(ttt(n:bin),Fratio(n:bin),'mo', 'MarkerFaceColor',[.49 1 .63])
xlabel('Time (s)','fontsize',12);
ylabel('Fisher Ratio','fontsize',12);
xlim([xl1 xl2])
ylim([0 80])

subplot(5,1,4)
plot(ttt(n:bin),phi(n:bin),'mo', 'MarkerFaceColor',[.49 1 .63])
ylabel('Back azimuth (deg)','fontsize',12);
ylim([0 360])
xlim([xl1 xl2])

ax3=subplot(5,1,3);
plot(ttt(n:bin),Capp(n:bin),'mo', 'MarkerFaceColor',[.49 1 .63])
ylabel('Apparent velocity (m/s)','fontsize',12);
ylim([200 500])
xlim([xl1 xl2])

subplot(5,1,2)
aa=n*binsize/2*ts;
bb=bin*binsize/2*ts;
tb=linspace(aa,bb,length(BestBeam));        %BestBeam for taking max value Fratio and shift
plot(tb,BestBeam)
ylabel('Pressure (Pa)','fontsize',12);
ylim([-8 4])
xlim([xl1 xl2])

subplot(5,1,1);
spectrogram(BestBeam,w,[],fspec,fs,'yaxis');
ylabel('Frequency (Hz)','fontsize',12)
xlim([(xl1-dif_s)/3600 (xl2-dif_s)/3600]);
set(get(gca,'XLabel'),'visible','off')
set(gca,'xtick',[]);
shading interp
%caxis          % check what the range is of your colorbar
caxis([-50 -0.7]);
set(gca,'Position',[0.1300,    0.8007,    0.7750,    0.1243]) % to get the same size as other
    subplots

toc
```

A-3 2D Frequency domain Fisher Analysis

```
% Frequency fisher analysis
```

```
clear
close all;
clc;

tic

%% read data
folder = '/run/media/woude/from_mos001_2tb/Thesis_3D_data/data/';
files = dir(fullfile(folder,'*.sac'));

numbgs=8;

        for il=1:numbgs
            x(il)=rdsac(files(il).name);
            raw(il,:)=x(il).d;
            time(il,:)=x(il).t;
            hdr(il,:)=x(il).HEADER;
        end

%% set parameters and visualize raw data
L = length(raw); % length of signal
fs= 40; % sampling frequency
ts = 1/fs; % sampling time
t = (0:ts:(L-1)*ts)';%calculate time axis
ninstr=size(raw,1);

        figure;
        for ii=1:ninstr;
        subplot(ninstr,1,ii)
        plot(t,raw(ii,:))
        xlim([0 7200])        %check where signal is located
        end

%% filter data
% butterworth frequencies
[b1,a1] = butter(1,[0.1/(fs/2) 5/(fs/2)],'bandpass');

% filter data and substracting mean (detrend)
figure;
[dat,X,samples]=deal(zeros(ninstr,L));
for ii=1:ninstr;
    dat(ii,:)=raw(ii,:)-mean(raw(ii,:),2);       % detrending before filtering
    X (ii,:)= filter(b1,a1,dat(ii,:));
    samples(ii,:)=X(ii,:)-mean(X(ii,:),2);       % detrending after filter
    subplot(ninstr,1,ii)
    plot(t,samples(ii,:))                        % visualise filter data for check
    xlim([2900 3000])
end

samples=samples';

%% load in coordinates
    A=load('/run/media/woude/from_mos001_2tb/Thesis_3D_data/coordinaten2.txt');
    rx=A(1:ninstr,2)-mean(A(1:ninstr,2));
    ry=A(1:ninstr,3)-mean(A(1:ninstr,3));

% define grid
    gridxy=50;

%% Parameters for fisher analysis

% set parameters
binsize=160;
N=ninstr;

%padding factor
pf=1;
Np=binsize*2^pf;

Nyquist=fs/2;
n=100/50;   %100%/50% overlap, choose your overlap
nbins=floor((length(samples)*2^pf)/(Np/n));
overlap=binsize/n;

% constants
kps=(1/(N^2));
kpt=(1/N);
lF=(N-1);

%frequency definition
freq=(0:(Np/2)-1)*Nyquist/(Np/2);
wn=-2*pi.*freq;
freqmin=0.1;
freqmax=3;
[~,ifmin]=min(abs(freq-freqmin));
[~,ifmax]=min(abs(freq-freqmax));
sf=ifmax-(ifmin-1);

% define Px and PY
[Px,Py]=deal(linspace(-0.005,0.005,gridxy));
```

```
[ep]=deal(zeros(ifmax,gridxy,gridxy,ninstr));
for f=ifmin:ifmax
    for ii=1:gridxy                                                          95
        px =Px(ii);
        for jj=1:gridxy
            py =Py(jj);

            for instr=1:ninstr                                               100
            dt= -(px*rx(instr)+py*ry(instr));
            ep(f,ii,jj,instr) = cos(wn(f)*dt)-1i*sin(wn(f)*dt);
            end
        end
    end                                                                      105
end

%% windowing
w=hann(binsize);
%w1=repmat(w,1,N); % if adding weights, otherwise set w1=1;                  110
w1=1;

%% Execute Fisher Analysis
[Ge]=deal(zeros(ninstr,1));
[Ftest]=deal(zeros(gridxy,gridxy));                                          115
[Fratio,phi,Capp]=deal(zeros((nbins-1),ifmax));
[save_I2,save_I3]=deal(zeros((nbins-1),sf));
[I2,I3]=deal(zeros(1,ifmax));
[tt]=deal(zeros(nbins,1));
                                                                             120
for bin=n:nbins-2
    ss=(bin-1)*overlap;
    es=ss+(binsize-1);
    tt(bin)=(ss+es)/2*ts;
        Gw=samples(ss:es,:).*w1;        % windowing adding weigths           125
      G=fft(Gw,Np,1);
      Gp=G(1:length(freq),:);

       for f=ifmin:ifmax
            PT=kpt*sum(abs(Gp(f,:)).^2,2);                                   130

            for ii=1:gridxy

                for jj=1:gridxy
                    Ge=zeros(ninstr,1);                                      135
                        for instr=1:ninstr
                        Ge(instr)=Gp(f,instr).*ep(f,ii,jj,instr);
                        end

                    PS=kps*abs(sum(Ge))^2;                                   140
                    Ftest(ii,jj)=(PS/(PT-PS))*1F;
                end
          end
     [Fratio(bin,f),I]=max(Ftest(:));
     [I2(f),I3(f)]=ind2sub([gridxy,gridxy],I);                               145

     % apparent velocity
        Capp(bin,f)=1/sqrt(Px(I2(f))^2 + Py(I3(f))^2);
     % back azimuth
        phi(bin,f)=atan2d(Px(I2(f)),Py(I3(f)));                              150
            if phi(bin,f)<0
                phi(bin,f)=phi(bin,f)+360;
            else
                phi(bin,f)=phi(bin,f);
            end                                                              155

        save_I2(bin,f)=I2(f);
        save_I3(bin,f)=I3(f);

      end                                                                    160
end

%% construction best beam
%set range if time window of signals is known because freq. analysis detects also other signals
[~,minbin]=min(abs(tt-2920));                                                165
[~,maxbin]=min(abs(tt-2960));

[~, posb]=max(max(Fratio(minbin:maxbin,:),[],2));
posbin=minbin+posb-1;
[Fmax,posf]=max(Fratio(posbin,:));                                           170
I2max=save_I2(posbin,posf);
I3max=save_I3(posbin,posf);

Pxbeam=Px(I2max);
Pybeam=Px(I3max);                                                            175
dtBB=-(Pxbeam.*rx+Pybeam.*ry);
dsBB= round((dtBB./ts));
start=binsize/n;     %starting place as time shift is the same
ssBB=start+dsBB;     %shifted samples with one Px and Py for all samples
esBB=es+dsBB;     %end shifted samples for all                               180
lBB=(esBB(1)-ssBB(1))+1;  % length of BBtest
```

```
[BBtest]=deal(zeros(lBB,ninstr));
for instr =1:ninstr
BBtest(:,instr)=samples(ssBB(instr):esBB(instr),instr); % time shift all samples
end

BestBeam=mean(BBtest,2);

%% plot figures
Capp(Capp>500) = 500;  % set limit, otherwise strange values

%define frequency for plotting
fff=freq(ifmin:ifmax);

%adjust time axis for better viewing signal
xl1=2850;
xl2=3090;

%selfmade colormap, use instead bv jet
load('mycmap.mat');

figure;
ax4=subplot(4,1,4);
pcolor(tt(n:bin),fff,Fratio(n:bin,ifmin:end)')
ylabel('Frequency (Hz)','fontsize',12)
xlabel('Time (s)','fontsize',12)
shading interp
colormap(ax4,hot(20))
ylim([freqmin freqmax]);
xlim([xl1 xl2]);
h=colorbar;
ylabel(h,'Fratio','fontsize',11)
caxis([0 120])

ax3=subplot(4,1,3);
pcolor(tt(n:bin),fff,phi(n:bin,ifmin:end)')
ylabel('Frequency (Hz)','fontsize',12)
shading interp
colormap(ax3,mycmap)
ylim([freqmin freqmax]);
xlim([xl1 xl2]);
h=colorbar;
ylabel(h,'Back azimuth (deg)','fontsize',11)

ax2=subplot(4,1,2);
pcolor(tt(n:bin),fff,Capp(n:bin,ifmin:end)')
ylabel('Frequency (Hz)','fontsize',12)
shading interp
colormap(ax2,redblue)
ylim([freqmin freqmax])
xlim([xl1 xl2]);
h=colorbar;
ylabel(h,'Apparent velocity (m/s)','fontsize',11)

ax1=subplot(4,1,1);
aa=tt(n);
bb=tt(bin);
tb=linspace(aa,bb,length(BestBeam));
plot(tb,BestBeam)
set(gca,'Position',[0.1300,    0.7673,    0.7250,    0.1577])
ylabel('Pressure (Pa)','fontsize',12);
xlim([xl1 xl2]);
ylim([-8 4]);

toc
```